Section 5

Development of and studies with regional and smaller-scale atmospheric models, regional ensemble, monthly and seasonal forecasting

Added value of high resolution for ALADIN Regional Climate Model

Michel Déqué and Samuel Somot
Centre National de Recherches Météorologiques, Météo-France.
42 avenue Coriolis F-31057 Toulouse Cédex 1, France, deque@meteo.fr

Limited area models have been first designed at 50 km resolution (Giorgi, 1990) and widely used at this horizontal resolution during 15 years (e.g. PRUDENCE European project, http://prudence.dmi.dk, Christensen and Christensen, 2007). Recently international projects target the 25 km resolution (e.g. ENSEMBLES European project, http://www.ensembles-eu.org) or even 10 km resolution (e.g. CECILIA European project, http://www.cecilia-eu.org).

Despite the huge cost of such models when their integration area is large, modelers expect to improve the simulations by getting more realistic surface forcings and by solving the continuous hydrodynamics equations with more accuracy. The result is not always convincing, since the physical parameterizations are generally developed, selected, and sometimes adjusted at lower (and less costly for tests) resolution. Another outcome of a higher resolution is the refinement of the output fields. Some details can appear at high resolution that are absent at coarser resolution. The most obvious example is surface elevation and, as a direct consequence surface temperature. Precipitation may also be improved, provided that the model does not over-simulate mountain forcing and that the model flow has the right direction.

There is a strong demand for regional details by climate impact users. However, given the chaotic behavior of the climate system, there is little chance that an impact simulated with 20 km accuracy by a scenario is a robust feature. From our experience, the agreement between members of ensemble scenarios if found at a much larger scale. However, if we can prove that the details provided by a regional model are in agreement with observation, we demonstrate that the spatial sensitivity of the model is correct. This increases our confidence in its sensitivity to other factors like greenhouse gas concentration.

The difficulty to evaluate the model capacity to resolve 10 km-scale details comes from the lack of high resolution homogeneous climate network. We have a high density of observations in some populated regions, but it hardly covers large areas. At Météo-France, an analysis system, named SAFRAN, has been developed in the 1980s for operational purpose. It has recently been extended back to 1970 and is maintained in real time (Quintana-Seguí et al., 2008). The data cover France on a 8km Lambert grid.

In order to evaluate the added value of using a high resolution model for simulating small spacial scales over France, two ERA40-driven simulations have been carried out with ALADIN. ALADIN is a limited area model used for short-range forecasting by a consortium of European and North-African countries (including Météo-France). It corresponds to a spectral version on a bi-periodicized Lambert grid of the global model ARPEGE (Bubnova et al., 1995). A climate version has been recently developed (Déqué and Somot, 2007). We use here version 4 of the climate model ARPEGE/ALADIN. Two versions on a relatively small domain (as compared with the EU-ENSEMBLES version) covering France have been designed. The first one has a 56 km grid on a Lambert projection centered at 47°N, 2°E with 50 latitudes by 50 longitudes. The second one has a 12 km grid on the same projection and 150 latitudes by 150 longitudes. The free (i.e. not Davies relaxed) part of the two integration domains corresponds to the same area covering France and a 200 km rim around the country. Both versions use exactly the same physical parameterizations (with the same time step, the same diffusion parameters, the same calibration parameters and the same source of soil characteristics). Each model has been integrated over the ERA40 period (1958-2001) and the mean climatology of the 1961-1990 period has been calculated. The two models have very similar systematic errors (somewhat too cold and too rainy), but no detrimental lateral boundary condition effect over France is seen in the precipitation field. One could have feared artificial numerical rainfall near the boarders, due to the small size of the domains.

Table 1 shows the spatial correlation over France of the simulated seasonal climatologies of 2m temperature and precipitation. The model land point data have been interpolated onto the 9304 land points of the SAFRAN grid with triangular interpolation (to minimize smoothing). The large-scale part of a field is obtained by replacing each local value by the spatial average in a 56x56km box centered on the grid point. The small-scale part is then the residual. The correlation is calculated separately for the large-scale and the small-scale parts. If we use raw temperature, ALADIN-12 km will obviously outperform ALADIN-56 km in the small scales because its finer orography. We have therefore used a 6.5 K/km vertical gradient to set the two models and the analysis at the sea level.

As far as the large-scale is concerned, both model have high correlation for temperature, the lower resolution version being slightly better. The precipitation correlation is less, and the higher resolution version is better. As far as the small-scale is concerned, the lower resolution has practically no skill: since the size of the box is the size of its grid mesh, the only small-scale features which remain are the changes in North-South or East-West gradients; these features are created by horizontal interpolation only. For precipitation and, to a lesser extent for temperature (winter and autumn only), the higher resolution version is able to produce relevant information inside the 56x56km boxes.

This result show that going from 56 km to 12 km resolution produces observation-related information. Linear interpolation from a coarser resolution is not equivalent.

		Temperature				Precipitation			
		DJF	MAM	JJA	SON	DJF	MAM	JJA	SON
LS	ALADIN 56 km	0.81	0.91	0.95	0.89	0.66	0.83	0.85	0.64
	ALADIN 12 km	0.79	0.88	0.94	0.86	0.74	0.90	0.92	0.74
SS	ALADIN 56 km	0.11	0.04	0.07	0.12	0.08	0.05	0.07	0.06
	ALADIN 12 km	0.40	0.04	0.06	0.33	0.50	0.54	0.47	0.52

Table 1: Spatial correlation over France for two versions of ALADIN versus SAFRAN analyses for seasonal mean temperature (elevation effects removed) and precipitation. Correlation is calculated separately for large-scale (LS, above 56 km) and small scale (SS, between 12 km and 56 km).

References:

Bubnová R., G. Hello, P. Bénard and J.F. Geleyn, 1995: Integration of the fully elastic equations cast in the hydrostatic pressure terrain-following coordinate in the framework of ARPEGE/Aladin NWP system. *Monthly Weather Review,* **123***,* 515-535.

Christensen, J.H. and O.B. Christensen, 2007: A summary of the PRUDENCE model projections of changes in European climate by the end of this century, Climatic Change, **81**, 7-30

Déqué, M. and S. Somot, 2007: Variable resolution versus limited area modelling: perfect model approach. *Research activities on atmospheric and oceanic modeling,* **37***,* 3.03-3.04

Giorgi, F., 1990: Simulation of regional climate using a limited area model nested in a general circulation model. *J. Climate,* **3**, 941-963

Quintana-Seguí, P., P. Le Moigne, Y. Durand, E. Martin, F. Habets, M. Baillon, C. Canellas, L. Franchisteguy, and S. Morel, 2008: Analysis of Near-Surface Atmospheric Variables: Validation of the SAFRAN Analysis over France. J. Appl. Meteor. Climatol., 47, 92–107.

The sensitivity of passive microwave responses to the hydrometeor properties simulated by a cloud resolving model in real rainfall systems associated with Baiu front

Hisaki Eito and Kazumasa Aonashi
Meteorological Research Institute, Japan Meteorological Agency
1-1, Nagamine, Tsukuba, Ibaraki, 305-0052, Japan
E-Mail: heito@mri-jma.go.jp

1. Introduction

Cloud Resolving Models (CRMs) with complicated cloud physical parameterization forecast various cloud physical variables with high resolution in time and space; therefore, CRMs serve as a valuable tool to be used in satellite remote sensing of precipitation for inferring information about clouds that cannot be directly observed. However, it is indispensable that CRM's outputs are verified with observational data to ensure the information being inferred from them is of the highest possible quality. Several observational data should be used fully to improve CRMs by estimating biases within the models and conducting needed adjustments to their physics and parameters to reduce those biases.

This study investigates the sensitivity of microwave brightness temperatures (TBs) simulated by a radiative transfer model to the hydrometeor properties simulated by CRM for the cloud microphysical validation of CRM. The sensitivity of simulated equivalent radar reflectivity (Ze) is also analyzed. TBs and Ze simulations are conducted for real rainfall systems associated with Baiu front around Okinawa Islands, Japan on 8 June 2004, which are compared to the timely corresponding satellite radiometer and grand-based radar observations, respectively Special attention will be given to the characteristics and sensitivities of CRM's ice hydrometeors forecasting.

2. Models

The CRM used in this study is JMA-NHM (Saito *et al.*, 2006), which is an operational nonhydrostatic mesoscale model developed by Japan Meteorological Agency (JMA). Rainfall systems associated with Baiu front has been simulated with double nested models, with a horizontal grid size of 5 and 2 km. In the inner model, explicit cloud microphysics scheme is only used as precipitation process. Results presented here are from the inner model only.

The bulk cloud microphysics scheme is employed in the JMA-NHM. This scheme predicts the mixing ratios of six water species (water vapor, cloud water, rain, cloud ice, snow and graupel) and number concentrations of ice particles (cloud ice, snow and graupel). The size distributions for each hydrometeors are represented by exponential functions. Mixing ratios and number concentrations are predicted for each ice particles, the slope and intercept of a given particle distribution are calculated, respectively.

Radiative transfer model (RTM) developed by Liu (1998) that used plane-parallel and spherical particle approximations is used for TBs simulations in this study. TBs are calculated for output from the JMA-NHM model simulations, compared to the timely corresponding AMSR-E observations on board Aqua.

3. Comparisons of simulations with observations

The JMANHM successfully reproduced the location and precipitation intensity of observed rainfall systems. The results of comparison of JMA-NHM simulation with AMSR-E observation. are shown in Fig. 1. Figure 1a shows the absorption index retrieved from 18 GHz data of AMSR-E. Colors varying from blue to red correspond to increasing absorption. The areas with large absorption index denote a large amount of liquid water in precipitation clouds. Simulated absorption index. is shown in Fig. 1c. In comparison with AMSR-E observation, the area with larger absorption index in simulation is a little smaller; however, the magnitude of simulated absorption index is in almost agreement with the observation. This result indicates that JMA-NHM well simulates the particle characteristics in liquid phase. Figure 1b shows the scattering index retrieved from 89 GHz data of AMSR-E. Colors varying from red to blue correspond to increasing scattering. The areas with large scattering index denote a large amount of ice hydrometeors. Figure 1d shows simulated scattering index. The location of the area with large scattering index is well simulated; however, the simulated scattering index is larger than observed one. This feature indicates that JMA-NHM overestimates an amount of ice hydrometeors.

The JMA-NHM simulation is also compared with ground based radar observations. Figure 2a shows a contoured frequency with altitude diagram (CFAD; Youter and Houze, 1995) computed by the radar reflectivity observed by NICT Okinawa Bistatic Polarimetric Radar (called COBRA). The highest probabilities follow a coherent pattern with the peak density steadily decreasing with height from between 25 and 35 dBZ near the melting level to between 10 and 20 dBZ near the strom top around 13 km. Below the melting level, peak probabilities are almost constant to the surface, indicating that evaporation is small. Figure 2b shows the simulated reflectivity CFAD. The highest probabilities also show a coherent pattern with the peak density like the observation. Below the melting level, there is an overall good agreement between the observation and the simulation. However, peak probabilities are shifted high between 4 km and 8 km, while low above 8km. Maximum simulated reflectivities around the melting level are higher than observed. This result indicates that the model accurately calculates the particle characteristics in liquid phase but overestimates the ice particle's size.

Investigation of profiles of simulated hydrometeors indicates that the dominant form of ice in this simulation is snow with much smaller amount of graupel and cloud ice (not shown). The overprediction of snow contents result in the overestimate of snow size, scattering index and radar reflectivity.

4. Sensitivity experiments

Comparison with radiometer and radar observation suggests the model overprediction of snow size. In this study, sensitivity experiments (named FVS and PSACW) are conducted that involved adjustments to the ice microphysical parameters that are important to snow growth.. In the FVS experiment, larger snowfall speed is used so that snow particles hardly remain in the air. In the PSACW experiment, riming threshold for snow to graupel conversion is reduced. Reducing this threshold favors more snow to graupel. In both sensitivity experiments, snow contents are reduced (not shown), indicating the both adjustments have a positive impact for reduction of snow content. In the experiment involved both adjustments (named FVS & PSACW), snow contents are significantly reduced from control experiment.

Figure 3a shows the reflectivity CFAD for the FVS & PSACW experiment, denoting some improvements over the control experiment shown in Fig. 2b. The improvement is the shift of probability from stronger echo to weaker echo between 4 km and 8 km above the melting level, and maximum reflectivities are also reduced around the melting level. However, the probability of reflectivities above 8 km is still lower than observation.

Figure 3b shows the scattering index retrieved from 89 GHz TBs for sensitivity experiment. The overestimate of the scattering index is reduced in the sensitivity experiment, reflecting the reduction of simulated snow diameters. However, despite the improvements of the sensitivity experiment, the simulated scattering index is still slightly higher than observation.

4. Summary

TBs and Ze simulations were conducted for real rainfall systems associated with Baiu front around Okinawa Islands, Japan, which were compared to the timely corresponding AMSR-E and COBRA radar observations, respectively. An almost good agreement is obtained between the simulated and observed TBs and Ze; however, JMA-NHM slightly overestimated a diameter of ice hydrometeors, especially a diameter of snow particles. The overestimation of snow diameters were reduced by some ice microphysical process adjustments of JMA-NHM such as larger snowfall speed and reduced riming threshold for snow to graupel conversion.

Additional cases will be analyzed to verify microphysical sensitivities of the model presented in this case and to improve the CRM and RTM by estimating biases within the models and conducting needed adjustments to their physics and parameters to reduce those biases.

Acknowledgments

This research was mainly supported by the fund of Japan Science and Technology Agency - Core Research for Evolutional Science and Technology.

Reference

Liu G. 1998: A fast and accurate model for microwave radiance calculations. *J. Meteor. Soc. Japan*, 76, 335-343.

Saito, K., T. Fujita, Y. Yamada, J. Ishida, Y. Kumagai, K. Aranami, S. Ohmori, R. Nagasawa, S. Tanaka, C. Muroi, T. Kato and H. Eito, 2006a: The operational JMA nonhydrostatic mesoscale model. *Mon. Wea. Rev.*, **134**, 1266-1298.

Yuter, S. E., and R. A. Houze Jr., 1995: Three-dimensional kinematic and microphysical evolution of Florida cumulonimbus. Part II: Frequency distributions of vertical velocity, reflectivity, and differential reflectivity. Mon. Wea. Rev., 123, 1941–1963.

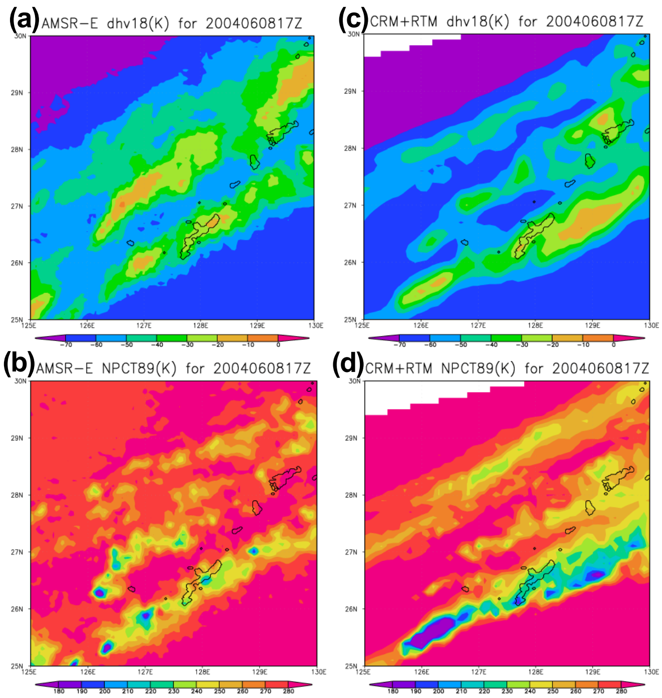

Fig. 1. (a) 18 GHz Absorption index and (b) 89 GHz scattering index retrieved from brightness temperatures observed by AMSR-E at 17 UTC on 8 June 2004. (c) 18 GHz Absorption index and (b) 89 GHz scattering index simulated by JMA-NHM at 17 UTC on 8 June 2004.

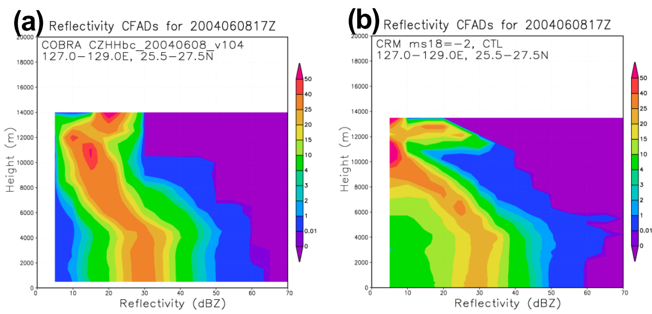

Fig. 2. Reflectivity CFADs in 127-129E and 25.5-27.5N at 17 UTC on 8 June 2004 derived from (a) observed CORBA radar reflectivity data and (b) the JMA-NHM simulation.

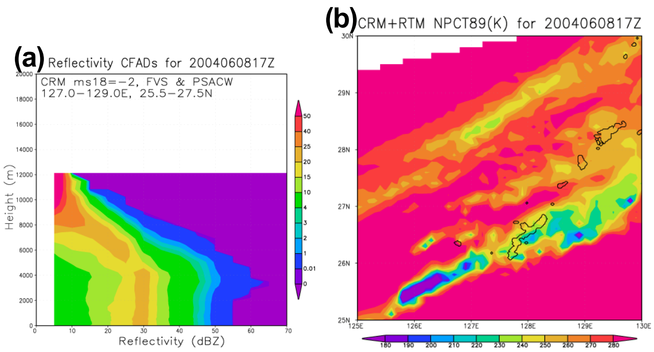

Fig. 3. (a) Reflectivity CFAD in 127-129E and 25.5-27.5N at 17 UTC on 8 June 2004 derived from the JMA-NHM sensitivity simulation (FVS & PSACW). (b) 89 GHz scattering index simulated by the JMA-NHM sensitivity simulation (FVS & PSACW) at 17 UTC on 8 June 2004.

Helicity as an indicator of tropical cyclone's intensity

Glebova E., Trosnikov I.
Ek.glebova@gmail.com
Hydrometeorological Centre of Russia

Tropical cyclones belong to the group of the most dangerous forces of nature. Their impact on the human life and infrastructure is due not only to the strong winds causing destruction but also to the abundance of consequences that may follow after their passage. It seems that tropical cyclones have already been completely investigated but in fact their behavior often remains obscure and even nowadays we can't give a perfect prediction of their formation and development.

One of the topical questions concerning tropical cyclones consider reasons of development or dissipation of tropical depressions. It can be useful for tropical cyclone prediction and for an active influence on typhoons at the stage of tropical depression. It's obvious that one can face plenty of difficulties while receiving observational data corresponding to the distribution of meteorological values in tropical cyclones (TC). That is why simulation of these severe storms turns out to be the only instrument of the exploration of their detailed structure.

In the aims of hurricanes' development simulation and calculation of several parameters of its intensity the mesoscale numerical model ETA was adapted to North-West Pacific and the Caribbean Sea (Mesinger, 1988, Black, 1994). ETA has 45 vertical levels and its horizontal grid's space is about 20 km. NCEP's analyse data with resolution 1° was used as initial and boundary conditions.

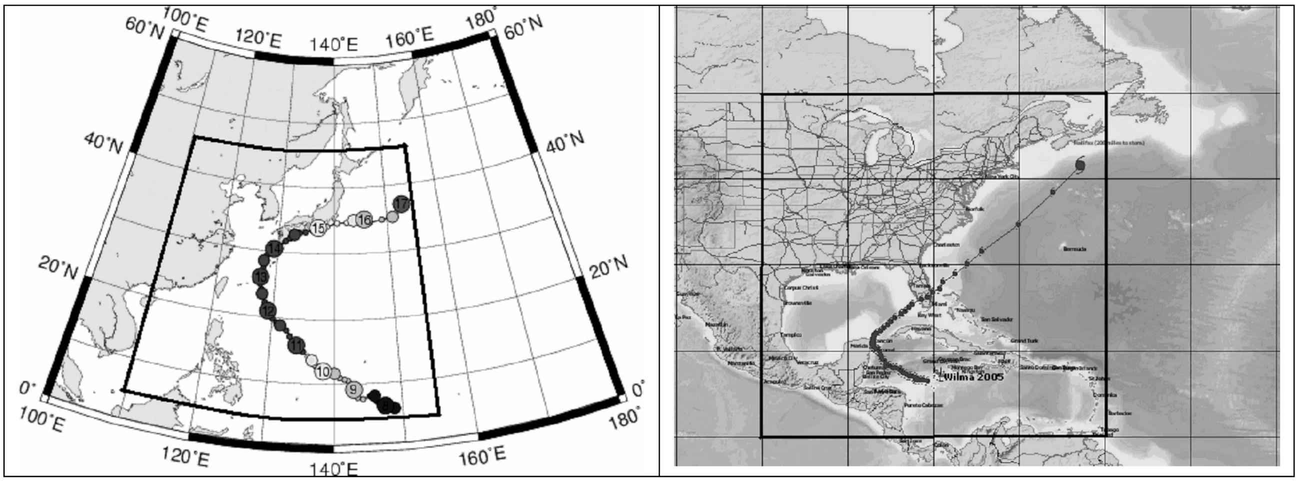

TC possess specific structure: a spiral circulation of air in it which is created by tangential and vertical circulation in the storm. The tangential circulation provokes great wind speed and the vertical is very important for heat and moisture exchange between the sea surface and the cyclone.

According to Kurgansky and Montgomery (2007), the downward flux of kinematic helicity across the top level of a turbulent viscous boundary layer can serve as an index of intensity and potential impact of atmospheric vortices such as tropical cyclone on the infrastructure:

$$SI = (8\pi/3)\int_0^\infty V^3 dr\ . \qquad (1)$$

Where*; r – radius, m; V(r) – azimuthal wind, m/s²; SI – downward flux of helicity, m³/s⁴*

We've calculated this value during the periods of tropical cyclones' development**.** The graphics for Man-Yi (2007, Pacific) and Wilma (2005, Atlantic) show that at the moment of intensifying of the cyclone, the index increases rapidly. The decrease is observed when a cyclone reaches the land and weakens or when it attaints higher latitudes. One can also notice the daily variation of helicity flux: at daytime it increases and at night the decrease is observed.

Davies-Johnes (1999) proposed to use relative helicity to estimate the force of the storm and reckon the storm motion in.

$$H = (V - Vmean)\frac{\partial u}{\partial z} + (U - Umean)\frac{\partial v}{\partial z}$$

Where V and U – meridional and zonal wind, m/s²; Vmean and Umean – meridional and zonal components of storm motion, m/s²; H – relative helicity, m/s².

As TC develops, relative helicity increases and its maximum is observed at the south-west part of the storm.

Man-Yi

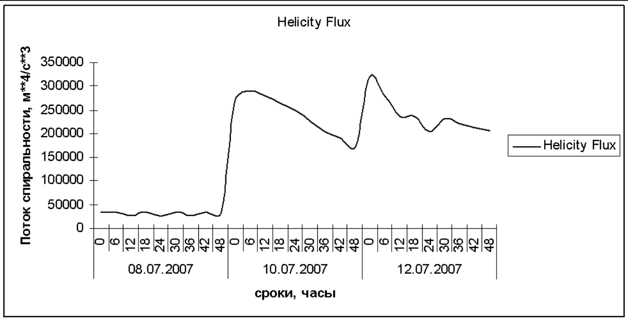

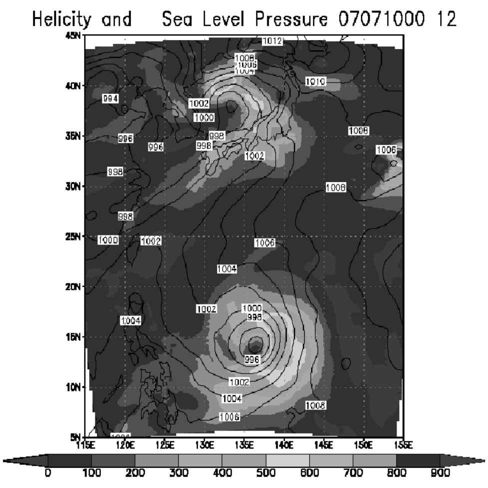

Wilma

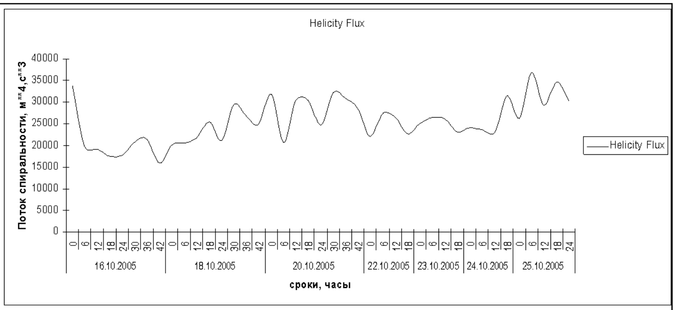

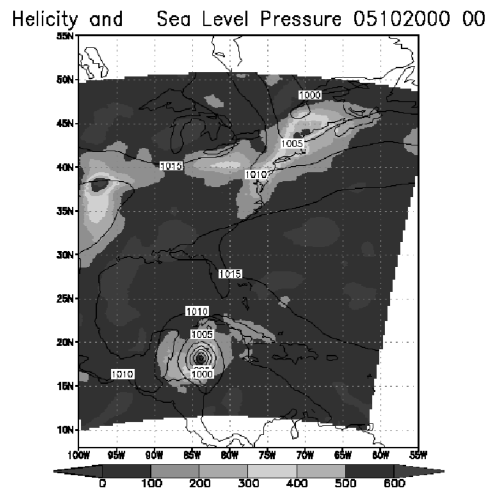

Replacement of lateral boundary condition in the operational meso scale model at JMA

Tabito Hara[1], Masami Narita, Ryoji Nagasawa, Daisuke Miura, and Yutaka Furuichi

Numerical Prediction Division, Japan Meteorological Agency, 1-3-4, Otemachi, Chiyoda-ku, Tokyo 100-8122, Japan

1 Introduction

MSM, the meso scale model at the Japan Meteorological Agency (JMA) with nonhydrostatic model (JMA-NHM), has been operated to issue information for disaster prevention (Saito et al. 2006, 2007). Its horizontal grid spacing is 5 km and it covers the region around Japan, 3600 km from east to west, 2880 km from north to south. Forecasts for 15 hours had been provided every 3-hours until May 2007, forecast period was extended to 33 hours 4 times among 8 times a day with considerable model improvements(Hara et al. 2007). This extension made it possible to deliver information to users up to 24 hours ahead.

Since MSM is a regional model, lateral boundary conditions are necessary to incorporate information outside of the domain. In MSM, the forecasts with RSM (Regional Spectral Model) had been used as the boundary condition since the beginning of its operation in Mar. 2001. On Nov. 21, 2007, RSM was replaced as the model providing the boundary condition by high resolution Global Spectrum Model (20-km GSM) at the same time with the start of the operation of GSM at JMA as the short-term weather forecasting model instead of RSM. GSM delivers its forecasts every 6 hours, while RSM did only twice a day. More frequent update of the boundary condition brings the advantage that MSM can use more accurate boundary condition because of its shorter forecast period and the latest observations assimilated through the analysis system.

In this report, we will present the performance of MSM with 20-km GSM forecasts given as the boundary condition, comparing it with the characteristics of 20-km GSM forecasts. It is confirmed that the performance of the inner model is strongly affected by the characteristics of the boundary condition.

Hereafter, MSM with the boundary condition provided by GSM and RSM are referred to as G-MSM and R-MSM, respectively.

2 New MSM system with 20-km GSM as the boundary conditions

Since Nov. 21, 2007, the forecasts predicted by 20-km GSM have been adopted instead of RSM as boundary conditions for MSM. The boundary conditions are updated every 6 hours corresponding to the update frequency of GSM. The other specifications of MSM are not changed from the previous upgrade in May 2007.

Note that the boundary conditions are also used in Meso-4DVAR analysis system. Although the model is influenced by 20-km GSM only in the boundary regions, the effects brought by 20-km GSM spread over the domain through the analysis cycle.

[1]E-mail: `tabito.hara@met.kishou.go.jp`

3 Statistical Verifications

To investigate the performance of G-MSM, experiments are conducted for one month for both in summer (Aug. 2004) and in winter (Dec. 2005 – Jan. 2006).

3.1 Vertical profiles

Fig.1 displays the vertical profiles of error statistics against the sonde observations over the MSM region. In the summer, the vertical profiles of root mean square error (RMSE) of geopotential height (Fig.1(a)), temperature, and wind speed (not shown) are improved more in G-MSM than R-MSM, which is attributed to the better performance of 20-km GSM than RSM from the view point of synoptic field. However, it also gives negative impact on MSM such as larger negative bias in vertical profiles of relative humidity (RH) (Fig.1(b)), which seems to be brought by 20-km GSM characteristics which has a considerable dry bias in the middle layer. In the winter, the geopotential height at upper layer around 250-300 hPa has an outstanding negative bias (Fig.1(c)), and the temperature has corresponding positive bias (Fig.1(d)), which are also under the influence of GSM characteristics.

3.2 Precipitation

There are no much differences in the threat score for predicting precipitation between G-MSM and R-MSM (Fig.2(a)). Special attention should be drawn to the increase of frequency to predict precipitation, especially heavy ones which can be recognized from the bias score (Fig.2(b)). It is considered to be brought by the excessive effect of the convective parameterization (Kain-Fritsch scheme) under the drier middle layer and moister lower layer, to which 20-km GSM has similar characteristics. One example of the cases in which precipitation is overestimated by G-MSM is displayed later.

3.3 Quality degradation with the forecast time advancing

As already mentioned, it is more advantageous for G-MSM that more frequently updated forecasts can be used as the boundary condition. Fig.3 shows the time series of threat score for precipitation predicted by G-MSM for each initial time. For several hours from each initial time, the best prediction can be obtained by adopting the latest one. However, in comparison with threat score between G-MSM of 15UTC initial time and G-MSM of 21UTC one, the quality of 21UTC is more rapidly degraded than 15UTC and the accuracy is almost the same in the latter part of forecast in spite of the shorter forecast time of 21UTC than one of 15UTC.

Presumably, the reason may be explained by the hypothesis that GSM of 06UTC and 18UTC initial

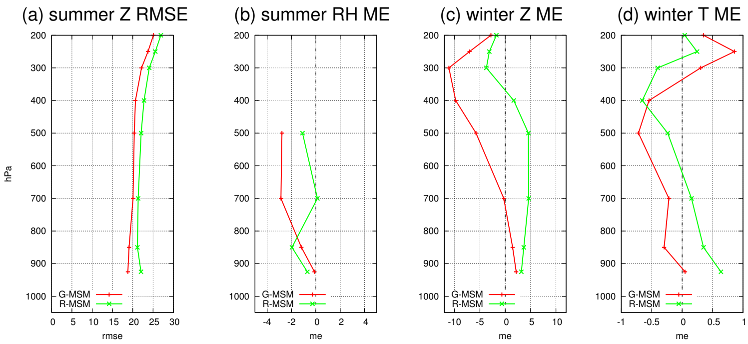

Fig. 1: Vertical Profiles of ME and RMSE. (a) RMSE of geopotential height (Z) [m] in the summer, (b) ME of RH [%] in the summer, (c) ME of Z [m] in the winter, and (d) ME of temperature [°C] in the winter. Green: R-MSM, Red: G-MSM.

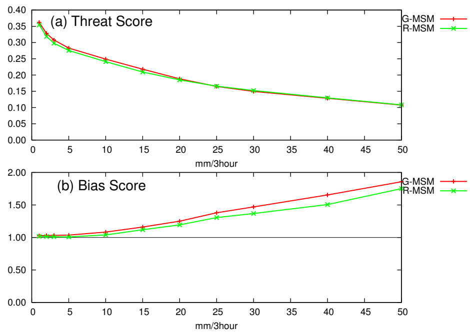

Fig. 2: Scores of precipitation prediction of each threshold. (a) threat score, (b) bias score. The transverse axis indicates threshold of precipitation [mm/3hour].

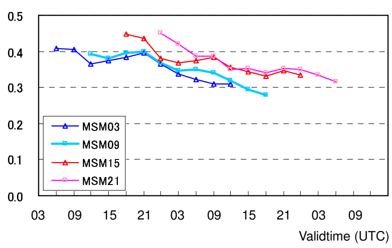

Fig. 3: Time series of threat score of precipitation with threshold of 1mm/3h for each initial time.

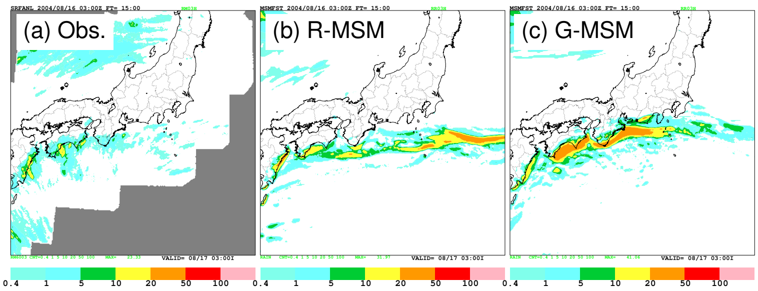

Fig. 4: 3-hour accumulated precipitation predicted with R-MSM and G-MSM, and its corresponding observation. Initial time is Aug. 16, 2004. Forecast time is 15 hours.

time is not as good as GSM of 00UTC and 12UTC due to the constraint of the operational system, in which the first guesses of the data assimilation of 00UTC and 12 UTC are generated by the analysis with more observations than 06UTC and 18UTC.

4 Problematic example predicted with G-MSM

Fig.4 shows the predictions with G-MSM and R-MSM, and the corresponding observation for the case on Aug. 16, 2004. In this case, weak precipitation was observed along the southern coast of Japan in association with the front. While R-MSM predicted similarly to the observation, G-MSM predicted too much precipitation intensity, which was mostly brought by the KF scheme, not grid-scale cloud microphysics. The lower layer in the south of precipitation area in G-MSM was much moister than R-MSM, and 20-km GSM used as the boundary condition of G-MSM had also the similar field to G-MSM, which suggests that G-MSM is considerably affected by moister field of 20km-GSM. It led to the overestimated precipitation by the KF scheme because the moister the lower layer, the more active the KF scheme works.

Although G-MSM do not always predict such excessive precipitation, frequency of it tends to be greater than R-MSM as the bias score of statistical verification (Fig.2(b)) indicates.

5 Conclusion

The boundary condition of MSM was switched to forecasts by 20-km GSM from that by RSM in Nov. 2007. Because of the better performance of 20-km GSM, some improvements are obtained. However, undesirable characteristics of 20-km GSM also affects MSM prediction, such as moist bias at lower layer, dry bias at middle layer, and positive temperature bias at upper layer, as well as the precipitation forecasts. To resolve these problems, 20-km GSM is highly expected to be improved. On the other hand, physical schemes in MSM should be also reviewed to adapt the different characteristics from the former boundary conditions.

References

Hara, T., K. Aranami, R. Nagasawa, M. Narita, T. Segawa, D. Miura, Y. Honda, H. Nakayama, and K. Takenouchi, 2007: Upgrade of the operational JMA non-hydrostatic mesoscale model. *CAS/JSC WGNE Res. Activ. Atmos. Oceanic Modell.*, **37**, 0511–0512.

Saito, K., J. Ishida, K. Aranami, T. Hara, T. Segawa, M. Narita, and Y. Honda, 2007: Nonhydrostatic Atmospheric Models and Operational Development at JMA. *J. Meteor. Soc. Japan*, **85B**, 271–304.

Saito, K., T. Fujita, Y. Yamada, J. Ishida, Y. Kumagai, K. Aranami, S. Ohmori, R. Nagasawa, S. Kumagai, C. Muroi, T. Kato, H. Eito, and Y. Yamazaki, 2006: The Operational JMA Nonhydrostatic Mesoscale Model. *Mon. Wea. Rev.*, **134**, 1266–1298.

Numerical experiment on the sensitivity of precipitation enhancement to cloud seeding position for the winter orographic cloud in Japan

Akihiro Hashimoto, Teruyuki Kato, Syugo Hayashi, and Masataka Murakami

Meteorological Research Institute, Japan Meteorological Agency

1. Introduction

Many research and operational projects in precipitation enhancement by cloud seeding are taking place in many countries. The effect of cloud seeding on surface precipitation should be dependent on the method of seeding. In the methodology of cloud seeding, it is important to choice the seeding material, seeding rate, and seeding position, adequately. Meteorological Research Institute (MRI), Japan Meteorological Agency (JMA) has been studying the feasibility of cloud seeding technique to enhance the winter snowfall in Echigo mountains which is the main reservoir for Tokyo metropolitan area. In this study, dry ice pellet is selected as a seeding material for its efficiency to induce the desirable change in the winter orographic cloud. The authors are studying the sensitivity of surface snowfall enhancement to the seeding position in order to find the optimal position to maximize the seeding effect, using the JMA's nonhydrostatic model (JMA-NHM; Saito *et al.*, 2006).

2. Model

The JMA-NHM has five categories of liquid and solid water substances: cloud water, rain, cloud ice, snow, and graupel, as described in Ikawa and Saito (1991). The two-moment bulk parameterization scheme, which prognoses both the mixing ratio and number concentration, is applied to the three categories of solid hydrometeor, while one-moment scheme, which prognoses only mixing ratio, is applied to the two categories of liquid hydrometeor, in this study. A cloud seeding scheme is newly implemented in the NHM so as to explicitly simulate the airborne seeding, deposition and fall of dry ice pellets, and generation of ice crystals.

3. Design of numerical experiment

a. Setup for simulation

The model domain covers the area of 200 km × 200 km centered at the dam catchment with a horizontal resolution of 1 km (1km-NHM), as shown in Fig. 1a. This domain is nested into the outer model which has the area of 1000 km × 1000 km centered at the offing of Niigata prefecture with a horizontal resolution of 5 km. The top height of the model domains is about 22 km. Fifty variable vertical layers are employed for both models. The regional analysis data (RANAL) provided by JMA were used as initial and boundary conditions for the outer model.

The initial time in 1km-NHM was set 3 hours after the initiation of outer model and the last 6-hour data in 9-hour integration time were used for analysis to avoid a spin-up effect. Control and seeding runs are conducted with the 1km-NHM. Cloud seeding is started at 2 hours after the beginning of seeding run, as shown in Fig. 1b. Seeding rate is set to 3 kg min^{-1} in the present study.

Corresponding author: Akihiro Hashimoto, Meteorological Research Institute, 1-1 Nagamine, Tsukuba, 305-0052, Japan. E-mail: ahashimo@mri-jma.go.jp

Table 1 Meteorological parameters in the 14 cases selected from two winter seasons of 2006 and 2007.

case	wind vector(U,V)	WS	LWP	T_{Q_c}	Q_c/Q_t	$Ttop$
200512251200	(22.6, -9.0)	23.9	0.147	-13.3	0.23	-20.1
200601101200	(7.2, -5.3)	9.8	0.063	-11.9	0.11	-20.7
200601171200	(14.5, -7.4)	15.9	0.114	-13.0	0.30	-14.2
200601221800	(14.5, -13.4)	19.1	0.098	-15.3	0.24	-17.5
200601250000	(10.9, -5.4)	12.3	0.111	-12.6	0.32	-14.0
200602031200	(12.8, -12.1)	16.7	0.064	-15.2	0.12	-22.7
200601220000	(21.7, -8.3)	23.6	0.095	-12.8	0.12	-25.3
200512120600	(4.6, -9.7)	11.6	0.095	-10.8	0.10	-27.9
200603060000	(12.4, -0.7)	12.7	0.253	-2.3	0.45	-22.1
200603281800	(20.3, -7.4)	21.1	0.093	-13.6	0.17	-11.0
200701101200	(12.4, -5.8)	13.6	0.259	-10.7	0.55	-13.2
200703121200	(21.9, -9.0)	23.2	0.305	-10.9	0.68	-12.3
200703170000	(7.9, -8.3)	11.1	0.096	-11.3	0.23	-13.8
200701070000	(23.8, -14.3)	27.3	0.284	-8.6	0.30	-21.7

where U and V (ms^{-1}) are the horizontal components of wind vector, WS (ms^{-1}) is wind speed, LWP (mm) is liquid water path, T (^{o}C) is cloud-water-mass-weighted temperature, Qc/Qt is mass ratio of cloud water to total water of hydrometeors, and $Ttop$ (^{o}C) is cloud top temperature.

b. Sensitivity experiment

In order to investigate the sensitivity of seeding effect to seeding position, at least 4 runs were conducted as well as a control run with changing the position of seeding with an 8-km interval along the search line directed upwind from Yagisawa dam. Figure 2 shows the arrangement of seeding positions along the search line indicated with the broken line AB in Fig. 1a. The flight level of seeding aircraft is assumed to be 2600 m roughly corresponding to the top of winter snow cloud in this area, except for over the high mountain area less than 16 km distant from Yagisawa dam where the flight level is assumed to be 3200 m since the cloud top becomes higher than over lower land. This sequence of simulations was performed for each of the 14 cases which are subjectively selected in two winter seasons so that the meteorological parameters in environment are dispersed over the possible ranges of their values. The search line changes so as to be along the environmental wind direction of each case. The meteorological parameters in environment are defined as those averaged over the rectangle area in domain2 of Fig. 1a and from 1- to 3-km height in the present study. The two winter seasons correspond to the terms from December 1, 2005 to March 31, 2006 and from December 1, 2006 to March 31, 2007. The selected cases are listed in Table 1.

4. Result

Figure 3 shows the examples of results from sensitivity experiments. It is found that the seeding effects on surface precipitation amount in dam catchment change depending on the distance from Yagisawa dam to seeding position. Although the interval of seeding position is relatively coarse, we assume that the optimal seeding positions to maximize the seeding effect are approximated by the positions of the

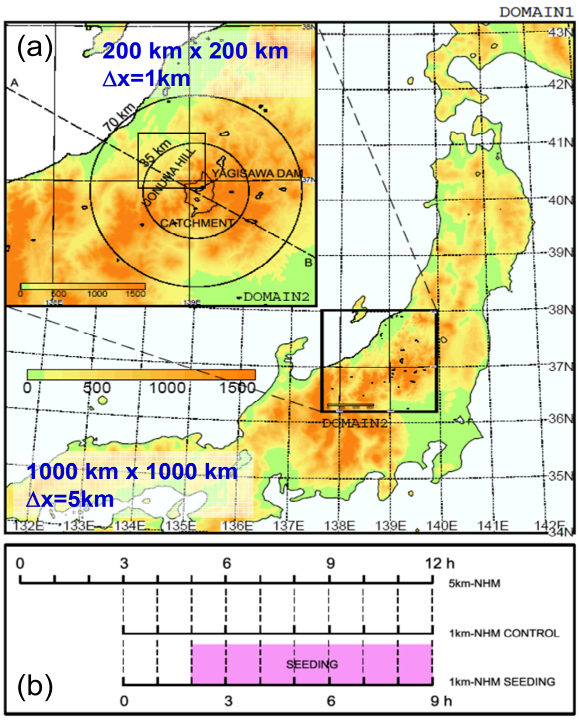

Fig. 1 (a) Calculation domains and (b) time integration sequences. The rectangle in domain 2 corresponds to the area over which the meteorological parameters are averaged to make the representative values of meteorological parameters in the environment.

maximum found in Fig. 3. Figure 4a shows the relationship between environmental wind speed and optimal seeding position in the 14 cases. It is found that the optimal seeding position has a correlation with the wind speed and that other factors independent of wind speed should have an effect as well.

$$y = \beta_0 + \beta_1 x_1 + \beta_2 x_2 + \beta_3 x_3 + \beta_4 x_4 + \beta_5 x_5 \qquad (1)$$

We applied a multi-linear-regression model with five variables (Eq. 1) to estimate the optimal seeding position based on meteorological condition, so that the optimal seeding positions in other cases can be estimated with the regression model. The five variables x_1 to x_5 in Eq. (1) are the environmental values of wind speed, liquid water path, cloud-water-mass-weighted temperature, mass ratio of cloud water to total water of hydrometeors, and cloud top temperature, respectively. The coefficients β_0 to β_5 in Eq. (1) are determined as 51.4, 4.08, -71.5, 3.73, -39.4, and 0.0885, respectively, as a result of regression analysis. Figure 4b shows the true optimal positions (black), same to those in Fig. 4a, and those estimated by the established regression model (grey). Differences between the true and estimated positions are found to be less than a couple of interval of seeding position in sensitivity experiments. The standard deviation of differences is 7.7 km. This is sufficiently smaller than the representative scale in the sensitivity of the seeding effect, namely, several tens km (Fig. 3), which indicates the efficacy of the regression model to estimate optimal seeding position.

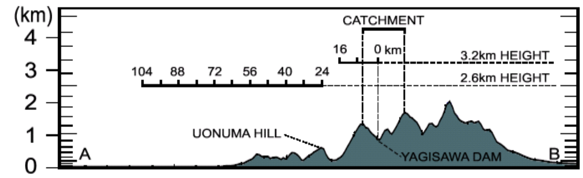

Fig. 2 Seeding positions along the broken line AB in Fig. 1a.

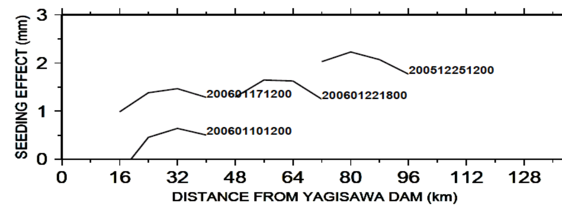

Fig. 3 Examples of results from sensitivity experiments. The ordinate indicates the seeding effect on surface precipitation in dam catchment. The abscissa indicates the distance from Yagisawa dam to seeding position. Number indicates the initial time (UTC) of outer model for each case.

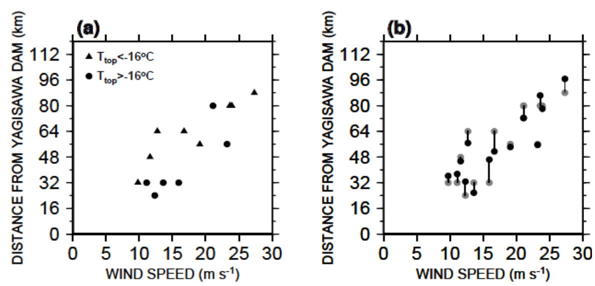

Fig. 4 (a) Relationship between environmental wind speed and optimal seeding position for the 14 cases. (b) Comparison between the true optimal seeding positions (black) and those estimated by multi-regression model (grey).

5. Summary

The regression model to estimate optimal seeding position is established in the present study. This model is based on only the 14 cases in two winter seasons. It should be verified if the regression model would well estimate the optimal seeding position for winter orographic cloud in many and unspecified cases. The dependence of seeding effect on the seeding rate should be investigated as well to make the optimal seeding technique more effective.

References

Ikawa, M. and K. Saito, 1991: Description of a nonhydrostatic model developed at the Forecast Research Department of the MRI. *Tech. Rep. MRI*, **28**, 238pp.

Saito, K., T. Fujita, Y. Yamada, J. Ishida, Y. Kumagai, K. Aranami, S. Ohmori, R. Nagasawa, S. Kumagai, C. Muroi, T. Kato, H. Eito, Y. Yamazaki, 2006: The operational JMA nonhydrostatic mesoscale model. *Mon. Wea. Rev.*, **134**, 1266–1298.

Simulation of Diurnal Variation of Planetary Boundary Layer Parameters over Western Ghats of India

Amit Kesarkar, Mohit Dalvi, Ancy Thomas and Akshara Kaginalkar
Computational Atmospheric Sciences, Centre for Development of Advanced Computing,
Pune University Campus, Ganesh Khind, Pune 411 007, India

1. Introduction:

A wide range of the atmospheric phenomena responsible for controlling the local weather conditions essentially have micro to mesoscale evolution. Even though these phenomena are greatly influenced by large-scale dynamics, they have direct and local interaction with mesoscale processes. These interactions are highly complex and their evolution in the free environment is determined by the underlying surface and its evolution. Topography is major factor which strongly modulates the exchange of energy and momentum between the surface and the overlaying atmosphere and is consequently responsible for spatial and temporal variability of the Planetary Boundary Layer (PBL) parameters such as mixing layer height, convective boundary layer height, and temperature lapse rates. The understanding of diurnal variations of these parameters is critical for prediction of the regional weather. To simulate their diurnal variation we have used Weather Research and Forecasting Model (WRF) developed by National Center for Atmospheric Research (NCAR), USA. The simulations using this model have been carried out for the period 11 – 19 April 2005 with the spatial extent of simulation domain as shown in Fig. 1. We have validated simulated surface temperatures for five synoptic meteorological stations of India Meteorological Department (IMD) viz. Mumbai (19^o 07' N, 72^o 51' E; 15 m), Goa (15^o 28' N, 73^o 54' E; 30 m), Cochin (9^o 57' N, 76^o 16' E; 3 m), Bangalore/ Bengaluru (12^o 58' N, 77^o 35' E, 920 m) and Pune (18^o 26' N, 73^o 55' E, 569 m), where the former four stations are RSRW observatories. Also, Mumbai, Goa and Cochin are located in the westward side of the Western Ghats separated by approximately 5^o latitudes and having low elevations. Pune and Bangalore are located on the eastward side (Fig 1) of Western Ghats and can be treated as hill stations. This study validates the simulated PBL structure by the WRF model over Western Ghats of India at these selected locations. The next section describes WRF model initialization and configuration while the results obtained from this work are discussed in section 3.

2. Model Initialization and Configuration:

WRF is a next generation, fully compressible, Euler non-hydrostatic mesoscale forecast model with a run-time hydrostatic option. The detailed description of WRF is presented in Wang et. al.(2004) and Skamarock et al (2005). For this study, two way nested computational domains of 70 X 105 X 40 and 85 X 197 X 40 grid points and horizontal resolutions of 32 km and 8 km respectively have been chosen (Fig. 1). The first domain covers most of the Indian subcontinent, ranging from 0 – 30^o N in latitude and 65 – 85^o E in longitude. The second domain covers the Western Ghats region of southern peninsular India ranging from 8 – 22^o N in latitude and 72 – 78^o E in longitude. The model is initialized by real boundary conditions using NCAR-NCEP's Final Analysis (FNL) data (NCEP-DSS1, 2005) having a resolution of $1^0 \times 1^0$ (~ 111 km x 111 km). The model is integrated for the period 11 – 19 April 2005 using a time step of 180 seconds. Other model configuration details are provided in table below.

Parameterization	Selected Scheme
PBL	Yonsei University (Hong et al, 2006; Hong and Dudhia 2003)
Surface Clay	Similarity theory (Paulson 1970; Dyer and Hicks 1970; Webb 1970)
Surface Physics	Noah (Chen and Dudhia, 2001)
Microphysics	Lin et al. (1983)
Cumulus Physics	BMJ (Janjic, 2000)
Long wave Radiation	RRTM (Mlawer et al., 1997)
Short wave Radiation	Dudhia (1989)

3. Results and Discussions:

Fig. 2 (a) shows the mean deviation of simulated surface temperatures using WRF model from observations recorded by IMD (NCEP-DSS2, 2005). It is seen that the deviation lies within ± 2^o C. The maximum positive departure is observed at Bengaluru at 1400 hrs UTC and the highest negative at Mumbai during the same time. It can be seen that Cochin, Goa and Pune show relatively less departure from observations. It is observed that the simulated surface temperatures follow similar diurnal trends with correlations of 92, 90.98, 92.38, 94.34 and 90.56 for Mumbai, Goa, Cochin, Bengaluru and Pune respectively. The standard deviations of simulated temperature are 4.05, 2.65, 2.24, 3.2, and 4.42 for Mumbai, Goa, Cochin, Bengaluru and Pune respectively. The positive (negative) temperature deviations can affect the values of PBL parameters, caused by an increase (decrease) in the Monin-Obukhov length (L), which in turn decreases (increases) the surface friction velocity (u^*) and convective velocity scale (w^*). However, the effect of this deviation on u^* and w^* is not expected to be significant as u^* varies inversely with the logarithm of L^{-1} (Panofsky and Dutton, 1984) and w^* varies with the cube root of temperature (Deardorff, 1970). The anomaly in the predicted temperature affects estimates of surface heat flux (HFX) and therefore the height of convective (CBL) and mechanical (Zm) boundary layer. Fig. 2 (b-d) shows the simulated HFX, CBL and Zm respectively. As seen from the figures, these parameters show similar behavior to that of surface temperatures. The magnitude of HFX ranges between 70 to 370 Wm^{-2} with minimum at Cochin and maximum at Mumbai. The values of peak CBL (Zm) range from 1000 (100) to 3500 (1000) meters with the above locations for maximum and minimum. The simulated CBL and Zm extend up heights of 3 Km and 1 Km respectively and show a reduction with decrease in the latitude. The ratio of latitudinal decrease in magnitude of these parameters from Cochin to Goa and Goa to Mumbai ranges between 2 to 3. Same is seen for Pune and Bengaluru. Even though Cochin, Goa and Mumbai are separated by about 5^o, the PBL parameters show more variability between the Goa to Mumbai than Cochin to Goa. This may be attributed to the march of the Sun from lower latitude towards Tropic of Cancer during this season.

1. Corresponding Author: Dr. Amit P Kesarkar, e-mail: akesarkar@cdac.in
Phone: +91-20-25704226 (O) Fax: +91-20-25694004

Acknowledgments: The help and suggestions provided by our colleagues from the Computational Atmospheric Sciences Team, C-DAC is thankfully acknowledged.

References:

Chen, F., and J. Dudhia, 2001: Coupling an advanced land-surface/ hydrology model with Penn State/NCAR MM5 model. Part I: Model description and implementation. Mon. Wea Rev, 129, 569–585.

Deardorff, J.W., 1970. Convective velocity and temperature scales for unstable boundary layer for Reyleigh convection. Journal of Atmospheric Sciences 27, 1211–1213.

Dudhia, J., 1989: Numerical study of convection observed during the winter monsoon experiment using a mesoscale two-dimensional model. *J. Atmos. Sci.*, **46**, 3077 – 3107.

Dyer, A., J., and Hicks, B. B., 1970. Flux gradient relationships in the constant flux layer, Quart. J. R. Met. Soc., 96, 715 – 721.

Hong, S.Y., Dudhia, J., 2003. Testing of a new non-local boundary layer vertical diffusion scheme in numerical weather prediction applications. In: 20th Conference on Weather Analysis and Forecasting/16th Conference on NWP, Seattle, WA.

Hong, S.Y., Noh, Y., Dudhia, J., 2006. A new vertical diffusion package with explicit treatment of entrainment processes. Monthly Weather Review 134 (9), 2318–2341.

Janjic, Z.I., 2000. Comment on development and evaluation of a convective scheme for use in climate models. Journal of Atmospheric Sciences 57, 3686.

Lin, Y. -L., R. D. Farley and H. D. Orville, 1983: Bulk parameterization of the snow field in a cloud model. *J. Climate Appl. Meteor.*, **22**, 1065 – 1092.

Mlawer, E. J., S. J. Taubman, P. D. Brown, M. J. Iacono and S. A. Clough, 1997: Radiative transfer for inhomogenous atmosphere: RRTM, a validated correlated – k model for long wave. *J. Geophys. Res.*, 102 (D14), 16663- 16682.

NCEP-DSS2, 2005. NCEP ADP Global Surface Observations, from Data Support Division (DSS), NCAR, Dataset # 464.0. /http://dss.ucar.edu/datasets/ds464.0

Paulson, C. A., 1970: The mathematical representation of wind speed and temperature profiles in the unstable atmospheric surface layer. J. Appl. Meteor., 9, 857–861.

Panofsky, H.A., Dutton, J.A., 1984. Atmospheric Turbulence: Models and Methods for Engg Appl. Wiley, New York, 417pp.

Skamarock, W.C., Klemp, J.B., Dudhia, J., Gill, D.O., Barker, D.M., Wang, W., Powers, J.G., 2005. A description of the advanced research WRF Version 2. www.mmm.ucar.edu/ wrf/users/docs/user_guide/ARWUsersGuide.pdf (access Sep 2006).

Wang, W., D. Barker, C. Bruyere, J. Dudhia and J. Michalakes, 2004: WRF version 2 modelling system user's guide. http://www.mmm.ucar.edu/wrf/users/docs/user-guide/.

Webb, E. K., 1970, Profile relationships: the log-linear range, and extension to strong stability, Quart. J. R. Met. Soc., 96, 67-90.

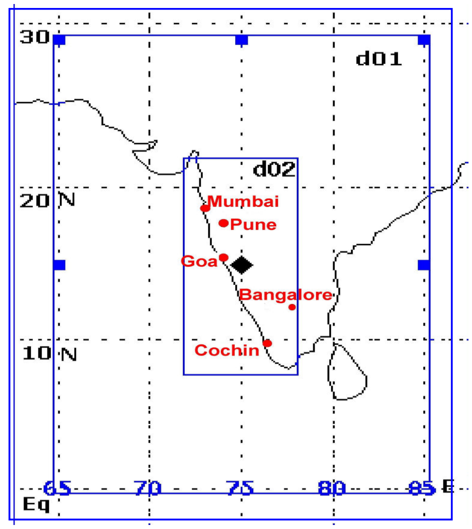

Fig –1: Domain for WRF simulation

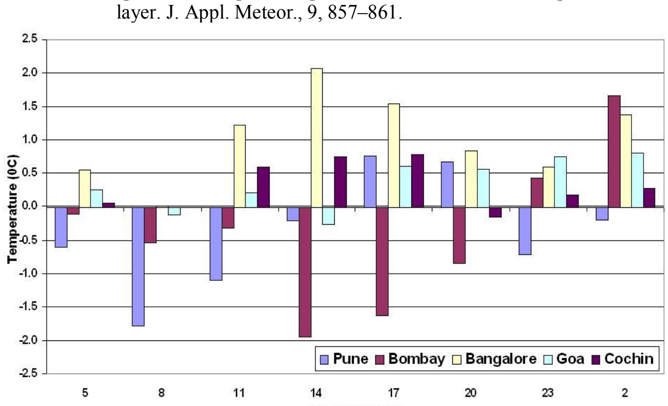

Fig-2(a): Mean Deviation of Surface Temperature from Observed

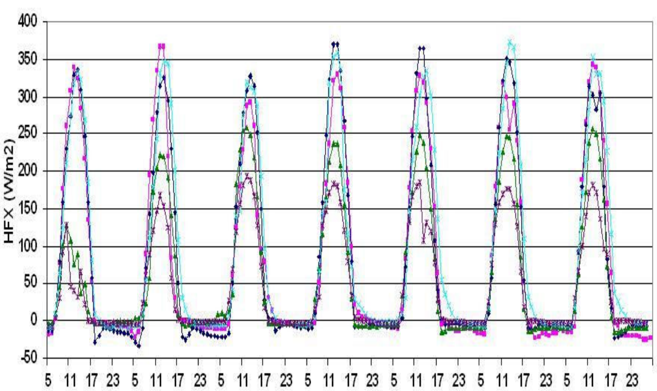

Fig- 2 (b): Surface Heat Flux

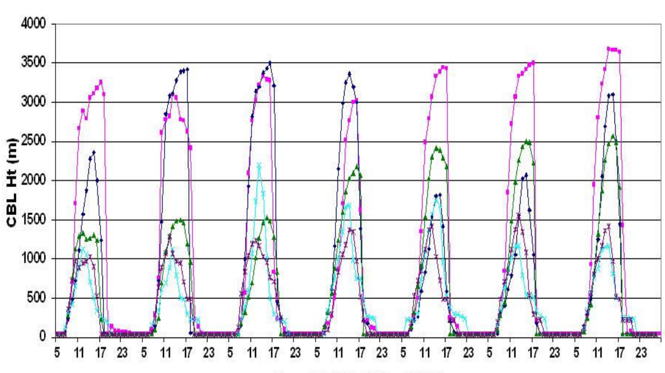

Fig-2 (c) Convective Boundary Layer Height

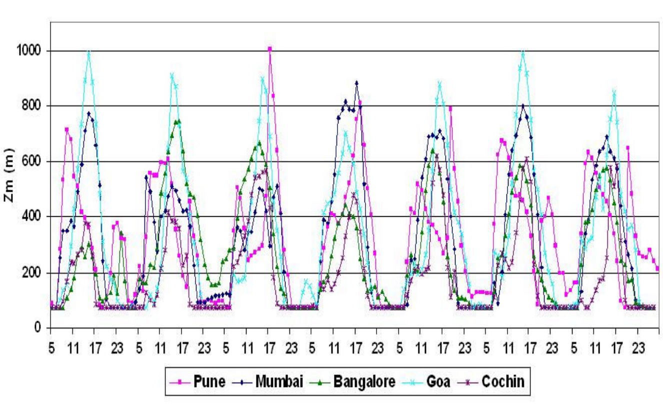

Fig-2 (d) Mechanical Mixing Layer Height

Verification of Experimental Quantitative Precipitation Forecast over Koyna Dam Catchment using WRF

Amit Kesarkar#, Akshara Kaginalkar, Basanta Kumar Samala, V. C. Shelke* and R.V.Panse**

Computational Atmospheric Sciences, Centre for Development of Advanced Computing, Pune University Campus, Pune 411007, India
**Koyna Project, Sinchan Bhavan, Mangalwar Peth, Pune 411011, Maharashtra, India*
***Superintending Engineer, Koyna Construction Circle,Satara, Maharashtra, India*

1. Introduction

The amount and pattern of precipitation over a given region is influenced by the orography, mesoscale precipitation processes occurring in the local atmosphere and large scale processes governing the local weather. The modeling of Quantitative Precipitation Forecast (QPF) over a mesoscale region is a very challenging task, however critical it may be. Koyna Dam is one of the largest dams in Maharashtra, India and a major hydro-electric power generation station. The complexity of the terrain of western ghats modulates the precipitation occurring over its catchment. The forecast of quantitative precipitation over Koyna dam region is crucial for controlling the water discharge efficiency. Therefore, in collaboration with Koyna Dam Authority, Irrigation Department, Govt. of Maharashtra we have issued an experiment QPF over Koyna Dam region during the period of 3rd August - 3rd October 2007 using Weather Research and Forecasting modeling system (WRF/ARW). The QPF were issued twice daily based on 00 (Evening Forecast) and 12 (Morning Forecast) UTC initial conditions. The results obtained from this experiments are discussed in this paper.

2. Model Configuration

WRF/ARW is a state of art modeling system developed by National Centre for Atmospheric Research (NCAR), Bolder, USA and described by Skamarock, 2005. WRF (ARW) version 2.2 is used in real time (www.rtws.cdac.in) to issue the QPF. Three two way nested computation domains of 277 X 184 X 27, 184 X 202 X 27 and 166 X 334 X 27 computational grid points with the resolution of 36 Km, 12 Km and 4 Km have been configured for the experiment. The model top is set at 10 hPa. The first domain covers most of South Asia and Indian subcontinent and is ranging approximately from 30^0 E to 130^0 E in longitude and 10^0 S to 45^0 N in latitudes. This domain captures the synoptic scale forcing responsible for the cumulus convection occurring over the Arabian Sea and the Bay of Bengal and majority of weather disturbances influence the weather over the Indian region for the period of 3 – 5 days. Other details of model configuration and initialization are presented in Table 1. The numerical output data processed to obtain the average amount of precipitation over Koyna catchment region and is compared with averaged observed precipitation of five rain gauge stations of the Irrigation Department in the catchment viz. Koyna, Navaja, Mahabaleshwar, Bamnoli and Pratapgad. The results are described in next section.

3. Results and Conclusions

Fig. 1 (a) and (b) show the quantitative precipitation forecast issued in morning and updated at evening based on 12 UTC initial conditions of previous day and 00 UTC initial conditions of same day respectively. As seen from this figure WRF is successful in simulating the average precipitation over Koyna dam region fairly well. However it is also seen that the point QPF for station needs higher resolution as well as improvement in representation of mesoscale processes in the model. It was observed that the 24 hour QPF issued in evening has less departure from observed than the QPF issued at morning hours. The scatter plot of observed 24 hour accumulated precipitation measured from 03 UTC of the day to 03 UTC of next day and 24 hour forecast are shown in Fig. 2 (a) and (b) for morning and evening forecast. These plots also show trend line of the precipitation and lines of 100 % more or less precipitation on both sides. It can be observed that by and large we can divide precipitation into three different categories viz. 0 – 20, 20 - 50 and more than 50 mm. The multi category validation of morning and evening forecast based on these categories are presented in Table 2. It can be seen that even though there are some "false alarms" none of the heavy precipitation event is missed by model. It can be seen that the number of false alarms are lesser in the evening forecast as compared to the morning one. This can be use to avoid the losses due to false alarm. The study shows further refinement of the QPF using statistico-dynamical techniques is required to increase value of the forecast.

Acknowledgments

The help and suggestions provided by our colleagues from the CAS Team of C-DAC are thankfully acknowledged. Authors are also thankful to Koyna Project Authority, Maharashtra Irrigation Department, Maharashtra, India for sponsorship for this research work and providing rainfall observations for the period of the experiments.

References:

Chen, F., and J. Dudhia, 2001: Coupling an advanced land-surface/ hydrology model with Penn State/NCAR MM5 model. Part I: Model description and implementation. Mon. Wea Rev, 129, 569–585.

Dudhia, J., 1989: Numerical study of convection observed during the winter monsoon experiment using a mesoscale two-dimensional model. J. Atmos. Sci., 46, 3077 – 3107.

Dyer, A., J., and Hicks, B. B., 1970. Flux gradient relationships in the constant flux layer, Quart. J. R. Met. Soc., 96, 715 – 721.

Hong, S.Y., Dudhia, J., 2003. Testing of a new non-local boundary layer vertical diffusion scheme in numerical weather prediction applications. In: 20th Conference on Weather Analysis and Forecasting/16th Conference on NWP, Seattle, WA.

Hong, S.Y., Noh, Y., Dudhia, J., 2006. A new vertical diffusion package with explicit treatment of entrainment processes. Monthly Weather Review 134 (9), 2318–2341.

Janjic, Z.I., 2000. Comment on development and evaluation of a convective scheme for use in climate models. Journal of Atmospheric Sciences 57, 3686.

Mlawer, E. J., S. J. Taubman, P. D. Brown, M. J. Iacono and S. A. Clough, 1997: Radiative transfer for inhomogenous atmosphere: RRTM, a validated correlated – k model for long wave. J. Geophys. Res., 102 (D14), 16663- 16682.

Paulson, C. A., 1970: The mathematical representation of wind speed and temperature profiles in the unstable atmospheric surface layer. J. Appl. Meteor., 9, 857–861.

Skamarock, W.C., Klemp, J.B., Dudhia, J., Gill, D.O., Barker, D.M., Wang, W., Powers, J.G., 2005. A description of the advanced research WRF Version 2. www.mmm.ucar.edu/ wrf/users/docs/user_guide/ARWUsersGuide.pdf (access Sep 2006).

Thompson, G., R. M. Rasmussen and K. Manning, 2004: Explicit forecast of winter precipitation using an improved bulk micro-physics scheme. Part I: description and sensitivity analysis. Mon. Wea. Rev., 132, 519-542.

Webb, E. K., 1970, Profile relationships: the log-linear range, and extension to strong stability, Quart. J. R. Met. Soc., 96, 67-90.

Corresponding Author: Dr. Amit P Kesarkar **e-mail:** akesarkar@cdac.in
Phone: 91-20-25704226 (O) **Fax:** 91-20-25694004

Table 1: WRF Model Configuration and Initialization

WRF Model Settings	Model Specifications
Domain	Indian Subcontinent, 30 E – 120 E / 10 S – 45 N
Resolution	36, 12, 4 km grid length, 27 vertical levels, 90 sec time step
Initialization and lateral boundary conditions	3 hourly boundary conditions using NCEP GFS system forecast (00 and 12 UTC analysis)
Physics Options	Microphysics: Thompson Scheme (Thompson et al, 2004) Cumulus Parameterization: Betts Miller Janjic (Janjic, 2000) Surface Layer: MM5 similarity (Paulson 1970; Dyer and Hicks 1970; Webb 1970) Land Surface Model: Noah LSM (Chen and Dudhia, 2001) Planetary Boundary Layer: Yonsei University (Hong et al, 2006; Hong and Dudhia 2003) Radiation: long wave: RRTM (Mlawer et al., 1997) Radiation: short wave: Dudhia (1989)
Objective Analysis & Data Assimilation	*3D Var (initial 3 hours, Nudging 00 / 12 UTC)* *GTS data (World Space + IAF)*
Forecast Duration Forecast Cycle	99 hours, output at each 15 minutes 00 and 12 UTC

Table 2: Verification of QPF issued with NCEP GFS initial conditions of 12 UTC of previous day (Morning Forecast and that of 12 UTC of same day.

Forecast \ Observed	0-20	20-50	>50	0-20	20-50	>50
	Morning Forecast			Evening Forecast		
0-20	16 (100%)	0	0	21 (96%)	1(4%)	0
20-50	6 (67%)	3 (33%)	0	8 (67%)	3 (25%)	1(8%)
>50	10 (26%)	10 (26%)	18 (48%)	5 (16%)	9 (29%)	17 (55%)

Red : Hit , Blue : Missed, Brown : False Alarm

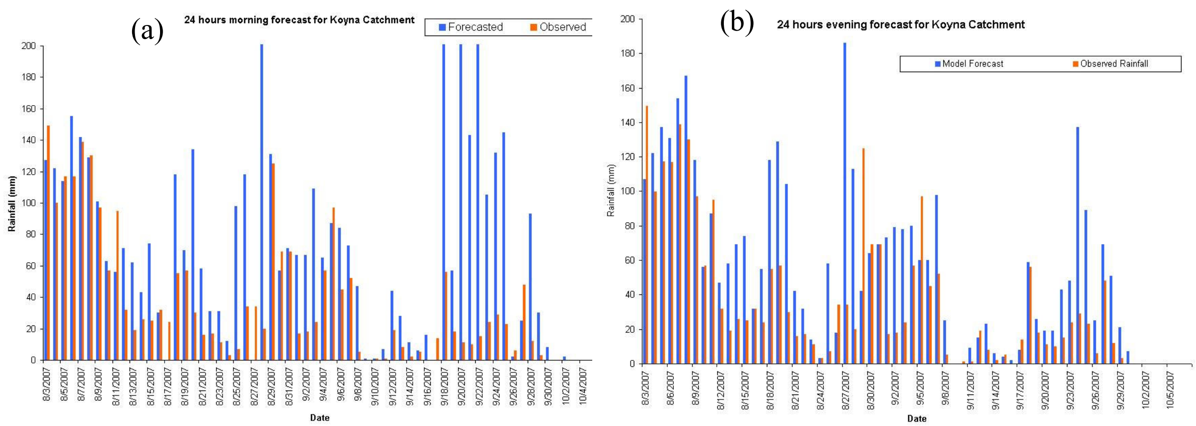

Fig. 1: Time Series of QPF and its comparison with averaged precipitation over Koyna Basin (a) Morning Time (b) Evening Time

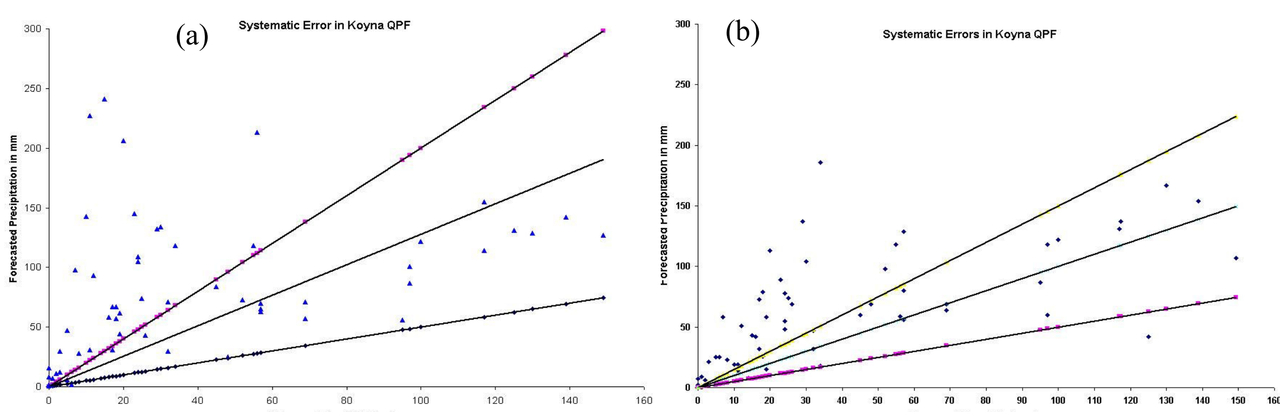

Fig. 2:Scattered plots of averaged observed precipitation over Koyna Dam region and QPF (a) Morning Time (b) Evening Time

Urban Heat Island over the Coastal City

I. Marinin and V.Shnaydman

Odessa State Ecological University (Ukraine), vives@matrix.odessa.ua
Rutgers-State University of New Jersey (USA), volf@envsci.rutgers.edu

The goal of this contribution is the quantitative description of the influence of the urban heat island and the large roughness on the atmospheric boundary layer structure over the sea-shore city. This aim is realized by combining the data of meteorological observations with atmospheric boundary layermodeling for Odessa (Ukraine) settled on Black Sea shoreline.

The urban dataset was obtained from a network of 8 remote sensors of the air temperature at 2 m height above the surface. It was completed by observations at 3 urban and suburban meteorological stations and 6 rural stations in the area of 50 x 50 km including 3 observational sites at the coast of the Black Sea.

We used the atmospheric boundary layer (ABL) model which included two- equation turbulence closure scheme [Shnaydman et all]. Appliance of the third level closure scheme with the turbulent kinetic energy and dissipation equations led undoubtedly to better and more detail construction of ABL structure especially when dealing with areas with a large horizontal variability of temperature and roughness.

Urban heat island (UHI) was detected as the area of higher (positive UHI) or lower (negative UHI) air temperatures over urbanized territory in comparison with suburban and rural ones. Naturally UHI is characterized with large roughness. In general a positive UHI was observed mostly in the evening (19 UTC). Mean temperature in the city was of 1,5–2 °C higher than in rural during the period of October-March and the largest intensity of the evening positive UHI got 4,6 °C in January. A positive UHI showed less intensity in the morning. The negative UHI was observed in April–September at 07 UTC when the urban area was 1,5–2 °C cooler than the rural one. The monthly mean intensity of the negative UHI got maximum 3,7 °C of the absolute difference values in July. The temperatures in the urban area were 1–1,5 °C higher (or lower) than the horizontal mean temperature of the calculation domain. Larger differences were observed for the small zones of the urban development.

The distribution of the wind velocity, temperature and turbulence parameters was calculated for 50x50 km domain, centered on the city. The contribution of urban heating and large roughness influence mechanisms on the ABL space structure over the coastal city was estimated from
the results of two numerical experiments.

The quantitative estimation of large roughness influence on the distribution of the wind and turbulence parameters was obtained in the first experiment. In this experiment the temperature on the 2 m was set by a constant horizontally averaged value in entire calculation domain. It allowed to exclude the urbanheat input and to evaluate theroughness contribution only.

The effective roughness lengths for the urban development were determined with the account of the building density and height. The distribution of the roughness lengths showed a large horizontal variability with a "plateau" of 0.5–0.7 m and "peaks" above 1.0 m abruptly falling down to the sea. Maximal urban roughness length was got as much as 1.7 m. In the rural area it was given with the value of 0.20 m.

The large values of the roughness created the increased values of friction velocity which were 0.25-0.40 m/sec. The amount of friction velocity increase in 1.2-1.5 times and roughness length rise in 2.5-3.5 times led to decrease the surface wind in 1.3-1.7 times. It lowered the wind blow along the streets and promoted the air pollution. The large values of the roughness essentially increased the parameters of turbulence. TKE were 0.4-0.6 m^2/sec^2 and 0.5-1.2 m^2/sec^2 accordingly in the rural and urban territories. The coefficients of turbulence were 1.5-2.5 times greater in urban place than in rural one and were equal 15-22 m^2 /sec. These results were obtained for the conditions of neutral stratification.

In the second experiment the modeling was initialized with the observed near-surface temperature field. The second experiment was resulted with the space distribution of meteorological fields and turbulence parameters due to the action of heating and roughness effects. The land–sea contrast of –5 °C and +9 °C were normally observed at 7 UTC and at 19 UTC. These contrasts produced a land breeze of 2–2.5 m s^{-1} and a sea-breeze of 5 m s^{-1}, respectively when the geostrophical wind was small. A positive UHI is typically non-stable with the maximal surface heat flux laid in limits 20–25 W/ m^2. The coefficients of turbulence and TKE were equal 25-40 m^2 / sec and 0.8-2.5 m^2/sec^2. The negative surface heat flux with 15-20 W/ m^2 absolute value was calculated for negative UHI . The coefficients of turbulence and TKE were equal 8-12 m^2 /sec and 0.4-1.0 m^2/sec^2. The ABL above the water area was stable.

Let's underline that the second experiment results reproduced the influence of horizontal gradients of temperature formed with the natural horizontal temperature differences and created with UHI contrasts. So the subtraction of the first experiment results from the second experiment ones allowed to obtain the baroclinic wind vectors. The introduction of the UHI with the intensity 7 °C produced the flow baroclinic component in the limits 1.0-1.5 m/s on 50 m .The negative UHI with the same intensity produced the baroclinic flow component in the limits 0.3-0.5 m/s on the same height. The layer of the UHI baroclinic flows is capped by 100 m.

The changes of turbulence parameters produced by the UHI contribution were different for positive and negative UHI. The positive UHI differences of TKE and turbulence coefficients were positive and the equal 0.3-1.3 m^2/sec^2 and 10-18 m^2 /sec. The negative UHI differences of TKE and turbulence coefficients were negative and their absolute values laid in the limits of 7-10 m^2 / sec and 0.1-0.2 m^2/sec^2.

In conclusion we would like to underline that quantitative description of the influence of the urban heat island on the seashore was obtained by using stationary 3-dimensional ABL model with two-equation turbulence closure scheme. The results given reassure that the developed approach can be successfully applied for the reconstruction of the temporal dynamics of ABL over the urbanized territory what is needed for the solution of the air pollution problem for the coastal cities.

Reference

Shnaydman, V., L. Berkovich, and S. Stepanenko 2006: Atmospheric Boundary Layer Modeling, *Ukrainian Hydrometeorological Journal*, No. 1, pp 2-27.

Numerical simulation of supercell tornadogenesis associated with Typhoon Shanshan (2006)

Wataru Mashiko
Meteorological Research Institute, JMA, 1-1 Nagamine, Tsukuba, Ibaraki 305-0052, Japan
(E-mail : wmashiko@mri-jma.go.jp)

1. Introduction

On 17 September 2006, three tornados hit the Miyazaki Prefecture in western Japan during the passage of the rainband which accompanied Typhoon Shanshan (2006). The tornado which hit Nobeoka city caused most severe damage, and it was assessed with F-2 scale. In order to investigate the environmental field, tornadic parent storm and tornado itself, the numerical simulations with high resolution were conducted (Mashiko 2007) using the nonhydrostatic model developed by Japan Meteorological Agency (Saito et al. 2006). The environmental field around which the tornado occurred was characterized by modest CAPE (~1000 J kg^{-1}) and strong low-level wind shear with veering. Some simulated convective cells in the outer rainband exhibited characteristics of a mini-supercell storm. They displayed differences from typical supercell storm on the Midwest in the U. S. with respect to the following points: 1) horizontal scale of the mesocyclone was smaller, 2) vertical vorticity was confined to lower levels (less than 5 km above ground level), and 3) near-surface temperature gradient around the gust front was slight (~1 K). When the mini supercell storm approached the coast of Nobeoka city, a tornado was successfully reproduced using the model with a horizontal grid spacing of 50 m. The simulated tornado with a diameter of about 500 m has about 1.0 s^{-1} vertical vorticity near the ground. Obviously, it is difficult to say that one is simulating the exact observed tornado at a given time and location. However, the simulation should be able to reproduce the representative type of the storms that would actually occur on this environmental field. Note that this simulation includes full-physics processes. Therefore, it is unlike the other previous studies employing free-slip surface condition. In this study, we will focus on the generation process of the tornado in the mini-suprecell storm.

2. Evolution of Low-level mesocyclone prior to tornadogenesis

Figure 1 shows the time-height cross section of maximum vertical vorticity and minimum pressure perturbation around the low-level mesocyclone center. The low-level mesocyclone in the mini-supercell storm is descending and intensifying with time. It subsequently connects to the tornado occurrence around 14:27 Local Time. The vertical vorticity reaches 1.0 s^{-1} near surface.

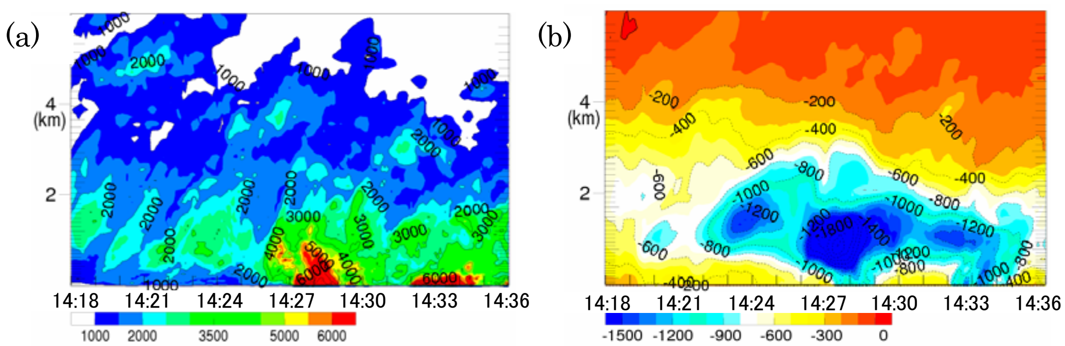

Fig. 1. Time-height cross section of (a) maximum vertical vorticity (× 10^{-4} s^{-1}), and (b) minimum pressure perturbation (Pa). Each value is calculated within a 2.5 km radius of mesocyclone center determined as the location of maximum vorticity on the 1km square averaged field at a height of 1 km.

3. Generation process of the tornado in the mini-supercell strom

As the low-level mesocyclone intensified, hook-shaped hydrometeors became prominent (Fig. 2a). Rrear-flank downdraft (RFD) associated with the hook-shaped hydrometeors was gradually intensifying and wrapping around the near-surface mesocyclone center (Fig. 2b). The tornado was generated between the left-front side of the RFD and the horseshoe-shaped updraft along the gust front (Figs. 2b and 2c). Actually, backward trajectories originating from the tornado show that about half of parcels traveled along the RFD (Fig. 3). When the RFD descended to the ground, it spread out and wrapped around the low-level mesocyclone. As it hit the leading edge of the rear-flank gust front, it could produce localized strong convergence and spin up the tornado.

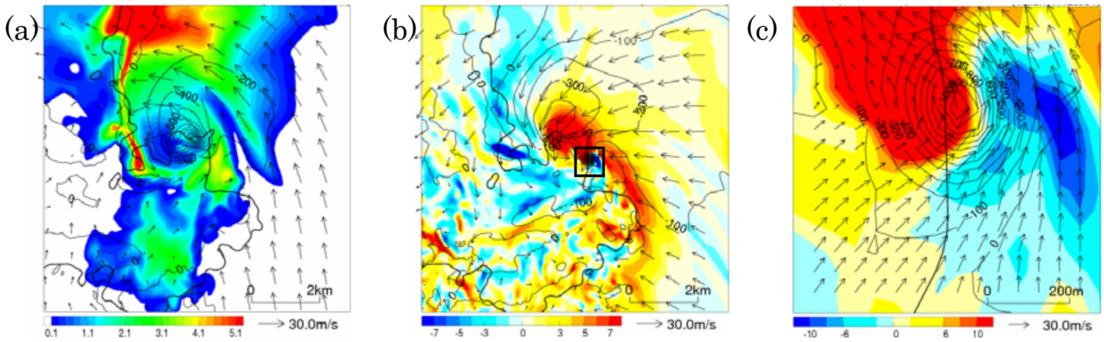

Fig. 2. Horizontal distribution of (a) hydrometeors (g kg^{-1}) at height of 1 km, (b) vertical motion (m s^{-1}) at a height of 250 m at 14:27 Local Time. (c) Enlarged display of the rectangle area in (b). Vectors depict storm-ralative winds. Contours indicate pressure perturbation (Pa).

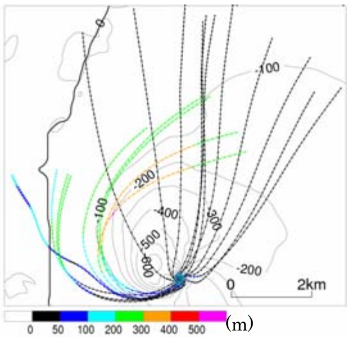

Fig. 3. Projection of the three-dimensional backward trajectories. Parcels were strated from the tornado location at a height of 150 m and integrated from 14:27 to 14:22. Colors of the trajectory path indicate the parcel height. Solid contours indicate the pressure perturbation (Pa) at origin time (14:27).

4. Sensitivity to the effect of evaporation cooling and precipitation loading

Sensitivity experiments were conducted to confirm the effect of evaporation cooling and precipitation loading on the RFD and tornadogenesis. In the experiment with no evaporation cooling, the behavior of the RFD and tornadogenesis were almost same as those of the control experiment. The evaporation cooling worked little unlike the typical supercell storm on the Midwest in the U. S. In the meanwhile, the RFD didn't wrap around the low-level mesocyclone and the tornado was not generated on the experiment in which the precipitation loading was neglected on the buoyancy term. Thus, the precipitation loading associated with the hook-shaped hydrometeors plays a key role in the RFD and subsequent tornadogenesis.

REFERENCES

Mashiko, W. 2007: Numerical simulation of tornado-producing supercell storm and tornado associated with Typhoon Shanshan (2006).

Saito, K., T. Fujita, Y. Yamada, J. Ishida, Y. Kumagai, K. Aranami, S. Ohmori, R. Nagasawa, S. Kumagai, C. Muroi, T. Kato, H.Eito, and Y. Yamazaki, 2006: The operational JMA nonhydrostatic mesoscale model. Mon. Wea. Rev., 134, 1266-1298.

Five years of COSMO–LEPS at ARPA–SIM

Andrea Montani, Chiara Marsigli, Tiziana Paccagnella

Hydro–Meteorological Service of Emilia–Romagna, ARPA–SIM, Bologna, Italy
corresponding author: amontani@arpa.emr.it

Introduction

COSMO–LEPS is the Limited–area Ensemble Prediction System developed and implemented by ARPA–SIM within COSMO (COnsortium for Small–scale MOdelling; the members of the Consortium are Germany, Greece, Italy, Poland, Romania and Switzerland). COSMO-LEPS project aims to generate "short to medium–range" (48–132 hours) probabilistic predictions of severe weather events based on the non–hydrostatic regional COSMO–model, nested on a number of ECMWF EPS members, chosen via a clustering selection technique (Marsigli et al., 2005). The "experimental–operational" COSMO–LEPS suite (following the methodology described by Montani et al., 2003) was set–up in November 2002 so as to produce probabilistic forecasts over a domain covering all countries involved in COSMO. After 5 years of activity, COSMO–LEPS application (now, an "ECMWF member–state time–critical application" managed by ARPA–SIM) is composed of 16 ensemble members, running at the horizontal resolution of 10 km with 40 model levels in the vertical. Perturbations to the initial and boundary conditions are provided by the different EPS members driving the limited–area integrations. In addition to this, the following model perturbations are introduced:
(1) perturbations to the convection scheme: within each COSMO–LEPS integration, a random choice between Tiedtke or Kain–Fritsche convection scheme is made;
(2) perturbations in the maximal turbulent length scale;
(3) perturbations in the length scale of thermal surface patterns.
In this contribution, it is assessed the state–of–the–art of the system, showing its ability to provide warnings of heavy precipitation events.

Results of verification

A big verification effort was undertaken so as to assess objectively how the system changed in its five years of activity and the extent to which modifications have actually improved precipitation forecasts over mountainous areas. In order to carry on this evaluation, a fix set of SYNOP stations (about 470) was selected, over an area covering the Alps (43-50N, 2-18E) and for the period ranging from December 2002 to November 2007. Precipitation accumulated over 12 hours (18-06 and 06-18 UTC) was verified, comparing the values forecast on the grid–point nearest to each station against the observed values at that station. As an example of COSMO–LEPS performance, Fig. 1 shows the time–series of the Brier Skill Score (BSS), for 4 different thresholds (1, 5, 10, 15 mm/12h) at the 78–90h forecast range (to increase readability, the 3–month running mean is actually shown). At the beginning of the verification period, the BSS is always negative, increasing to positive values at least for the lower thresholds starting from summer 2004. The BSS is steadily positive from spring 2005, for all the thresholds except the highest (15mm/12h). A different behaviour is exhibited in autumn 2006, which was a very dry season: COSMO–LEPS performance is not satisfactory. On the other hand, the BSS is almost always above zero throughout 2007 for most thresholds, indicating a skillful system in the prediction of precipitation at the day–4 range. A marked seasonal variability is also evident, the system often performing better in the summer season. In the overall evaluation of the

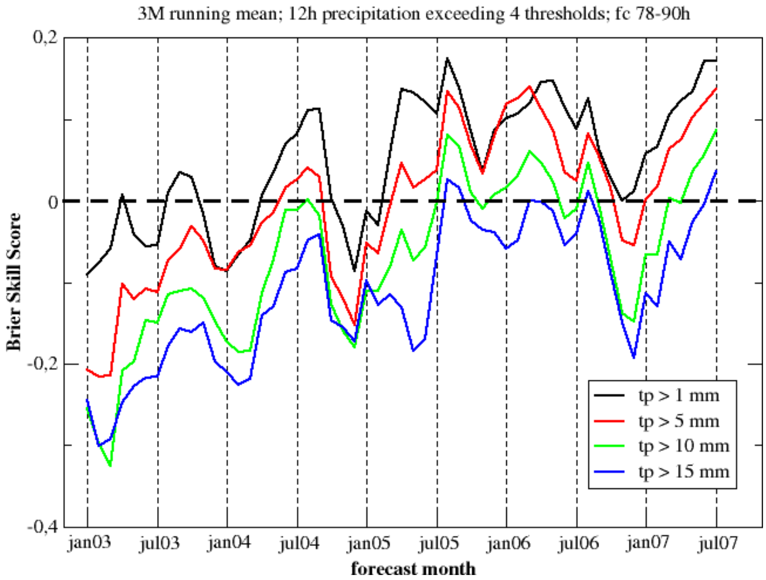

Figure 1: Forecast range 78–90h: Brier Skill Score time–series (from January 2003 to July 2007) for COSMO–LEPS 12-hour precipitation exceeding 1,5,10,15 mm. The BSS is computed for each month. A 3-monthly running mean is applied to improve the readability.

system performance, it has to be kept in mind that, in addition to the upgrades in the COSMO–model itself, COSMO–LEPS configuration was subject to two major changes during the verification period:
(1) June 2004: the ensemble members were increased from 5 to 10 and only two EPS instead of three were considered to select the global–model members to drive the COSMO–LEPS integrations.
(2) February 2006: the ensemble members were increased from 10 to 16 and the vertical resolution of COSMO–LEPS integrations from 32 to 40 levels.
The former change seems to have led to better scores, since an improvement is evident from spring 2004. The impact of the latter change is more difficult to be judged, due to the already underlined problem in autumn 2006. Nevertheless, a positive trend is evident in the scores obtained during 2007, especially in view of the various meteorological experiments which took place during that year (e.g. COPS and MAP D-PHASE). This is even more true if other scores, like the area under the ROC curve and the percentage of outliers, are considered (not shown). Nowadays, COSMO–LEPS products are well–established in met–ops rooms within COSMO community. They have been recently used with success in EC projects (e.g. Windstorms PREVIEW) as well as in the field campaigns of the above–mentioned meteorological experiments. As future developments, it is planned to introduce more model perturbations, so as to improve the spread–skill relationship of the system, and to develop “calibrated” COSMO–LEPS forecasts.

References

Marsigli C., Boccanera F., Montani A., Paccagnella T., 2005. The COSMO-LEPS mesoscale ensemble system: validation of the methodology and verification. *Nonlin. Proc. Geophys.*, **12**, 527–536.

Montani A., Capaldo M., Cesari D., Marsigli C., Modigliani U., Nerozzi F., Paccagnella T., Tibaldi S., 2003. Operational limited–area ensemble forecasts based on the ‘Lokal Modell’. ECMWF Newsletter No. 98. Available from: ECMWF, UK.

Numerical simulation of severe weather events in South/Southeast Asia using NHM

Hiromu SEKO*, Syugo HAYASHI, Masaru KUNII and Kazuo SAITO
Meteorological Research Institute

1. Introduction Severe disasters, e.g. heavy rainfall, flood, ground slide, frequently occur in Southeaster Asia. On the other hand, JMA has developed the NHM, and then NHM has been used as operational model to predict the severe phenomena in and around Japan. In this report, numerical simulations of the strong wind and heavy rainfall events were performed by using NHM of JMA to investigate the usefulness of it for the prediction of weather phenomena in the tropical region. Preliminary results on these events will be presented.

2. Strong wind event First event is the strong wind on 29 November 2006 over the Java Sea. A ferryboat was wrecked by the strong wind and high waves, and more than 500 people were claimed. Sea surface wind speed and rainfall intensity when the ferryboat was in distress were observed by AMSR-E (Fig. 1). The wind and rainfall intensity near the accident scene exceeded 20 m/s and 30 mm/hour, respectively (http://www.eorc.jaxa.jp/imgdata/topics2007/tp07024.html). The strong wind event was simulated by NHM with the grid interval of 5 km. The JMA global analysis data were employed for the initial and boundary conditions. A low-pressure system developed south of the Java Island, and then westerly flow intensified by this low pressure system expanded eastward over the Java Sea (Fig. 2). Strong wind region moved to the north of Bali by 16 UTC 29, and then the wind speed at the height of 20 m reached the maximum speed of 27 m/s. A convective region is seen in the Java Sea, while this cluster seems not to much affect the simulated strong wind because it was located far from the strong wind region.

3. Heavy rainfall event Second event is the heavy rainfall occurred at Mumbai on 26 July 2005 (Bohra et al, 2005). Rainfall more than 900 mm/day was observed at Santa Cruz, a suburb of Mumbai (Fig. 3). Although this heavy rainfall occurred at the localized area of 20-30 km, rainfall system that produced the intense rainfall lasted for more than 6 hours. This heavy rainfall was also simulated by NHM with the grid interval of 5 km using the JMA global analysis data. Localized intense rainfall was reproduced near Mumbai while relatively weak rains (less than 10 mm/hour) were generated along the southern coastal line (Fig. 4). Because the heavy rainfall was developed at the coastal line near Mumbai, the topographic effect seems to be essential for its generation. As the convection of the heavy rainfall was developing, the surface pressure near the convection decreased. This drop of the surface pressure intensified the convergence, and maintained the heavy rainfall. As for the horizontal flow around the heavy rainfall, the zonal wind reverses its direction as the height increases. These airflows around the heavy rainfall were favorable to stay the heavy rainfall near the Mumbai.

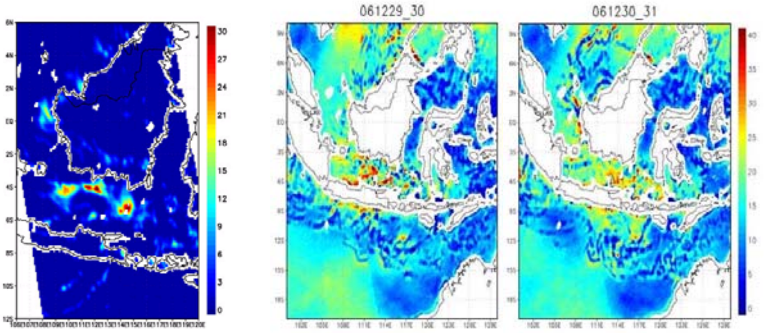

Fig.1 (left) Rainfall intensity and (right) surface wind velocity observed by AMSR-E (From home page of JAXA).

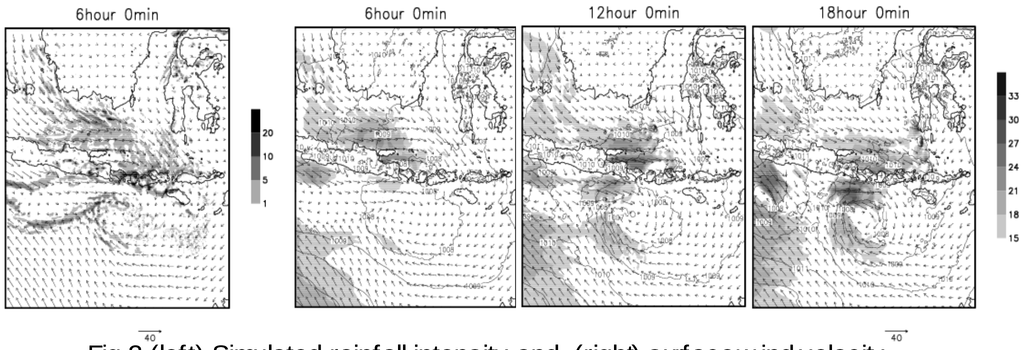

Fig.2 (left) Simulated rainfall intensity and (right) surface wind velocity.

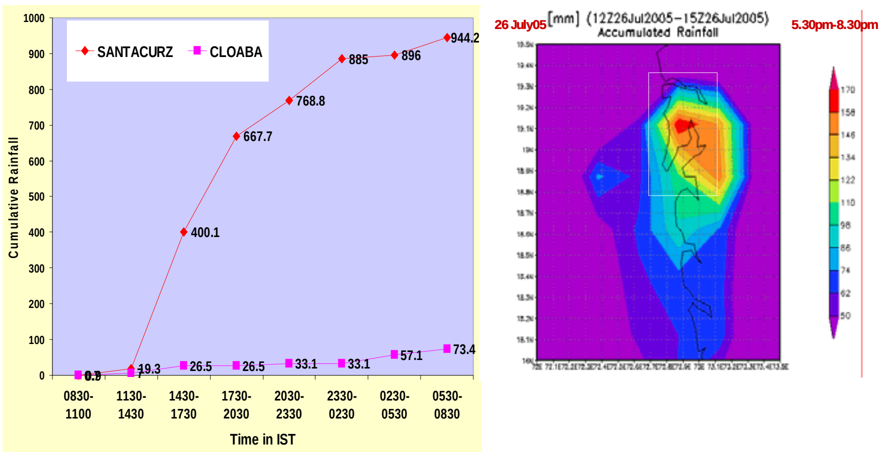

Fig.3 (left) Accumulated rainfall at SANTACURZ and rainfall distribution observed by TRMM (from fig.1 and fig.2 in Bohra et al. 2005).

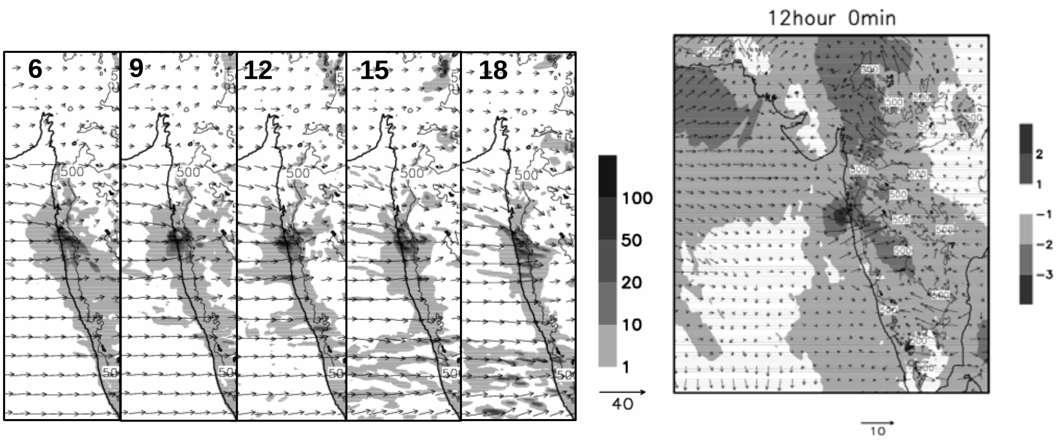

Fig.4 (left) rainfall distribution from FT =6 hour to 18 hour, and (right) the increments of surface pressure and horizontal wind at FT=12 hour from the initial condition.

Experimental operation of a high-resolution local forecast model at JMA (2)

Kensuke Takenouchi, Haruka Kurahashi, Tadashi Fujita and Kohei Aranami
Numerical Prediction Division, Japan Meteorological Agency,
1-3-4 Otemachi, Chiyoda-ku, Tokyo 100-8122, Japan
E-mail: k.takenouchi@met.kishou.go.jp

1. Introduction

Since 01 June 2006, an experimental operation of a high-resolution Local Forecast Model (LFM) has been executed 3-hourly (8 times a day) to produce forecasts for 12 hours. The horizontal grid spacing of the LFM is 2 km at present. And the initial condition is prepared by a rapid update cycle with the 3D-Var version of JNoVA*[1]. (Nakayama et al. 2007, hereafter N07)

This report describes the refinements after N07, presents the verification results in 2007 and discusses some remaining issues.

2. Refinements after N07

On 16 May 2007, the operational meso-scale model (MSM) was improved (Hara et al. 2007). The same improvements were basically applied to the LFM. In addition, convective parameterization was applied as explained in Section 4 (i) on 01 June 2007.

3. Verification results

The verification results for the period from June 2007 to December 2007 are presented in this report. Figure 1 shows the bias score and the equitable threat score of precipitation forecasts against the Radar-raingauge Analyzed Precipitation and Figure 2 shows the mean error and the root mean square error of surface temperature and wind speed forecasts against the surface observations (AMeDAS *[2]). The verification results of the MSM, which prepares the boundary condition for the LFM, are presented to compare with the LFM.

The bias score (BS) of precipitation on the average shows that the LFM produces heavy precipitation (> 15 mm/hr) excessively and this tendency is stronger than that for the verification period of N07. Meanwhile, the BS of precipitation on the maximum is closer to 1 than that of N07.

The mean error (ME) of surface temperature shows that the LFM has a negative bias in the day time and a positive bias in the night time, and the root mean square error (RMSE) of the LFM is smaller than that of the MSM almost throughout the day. As for surface wind speed, both the ME and the RMSE are almost the same between the LFM and the MSM.

4. Issues

(i) excessive rainfall in grid point scale

In summer 2006, excessive rainfalls in grid point scale had occasionally happened. Figure 3 shows one example (03 UTC on 08 September 2006). The organized convections developed in the southern sea area of the experimental domain. To cope with this problem, a modified version of the Kain-Fritsch scheme for the LFM has been temporarily applied to the experimental run since 01 June 2007. However, even with this scheme, the LFM still produces heavy rains more excessively as described in Section 3. Therefore, we are investigating the need for convective parameterization and seeking an appropriate scheme for the LFM at the present.

(ii) Background error covariance in the analysis system

The background error covariance in the analysis system is produced by the NMC method (Parrish and Derber 1992), which uses the differences between 6-hour and 12-hour forecast by the MSM. However, it is likely that the calculated correlation length scales of background error are too long. As a result, the influence of each assimilated observations extends over a very large area. Figure 4 shows one example (09 UTC on 29 October 2007) of this problem. Although there were no assimilated observation data on sea surface, the increment spread over sea far from land surface observation points. We need to find an optimum background error covariance for the LFM system, for example, by introducing spatial inhomogeneities and anisotropies into the covariance.

Additionally, the assimilation of new data such as MTSAT-1R AMV, Ground-based GPS, retrieved ATOVS, SYNOP and Upper Soundings is considered.

Reference

Nakayama, H., Y. Ishikawa, T. Fujita and K. Takenouchi, 2007 : Experimental operation of a high-resolution local forecast model at JMA. *CAS/JSC WGNE Res. Activ. Atmos. Oceanic Modell.*, **37**, 0519–0520.

Hara, T., K. Aranami, R. Nagasawa, M. Narita, T. Segawa, D. Miura, Y. Honda, H. Nakayama, and K. Takenouchi, 2007: Upgrade of the operational JMA non-hydrostatic mesoscale model. *CAS/JSC WGNE Res. Activ. Atmos. Oceanic Modell.*, **37**, 0511–0512.

Parrish, D.F. and J.C. Derber, 1992: The National Meteorological Center's spectral statistical interpolation analysis system. *Mon. Wea. Rev.*, **120**, 1747–1763.

----

*[1] JNoVA is Japan Meteorological Agency (JMA) Non-hydrostatic Model based Variational Data Assimilation System.

*[2] AMeDAS (Automated Meteorological Data Acquisition System) is a high-density surface observation network covering Japan.

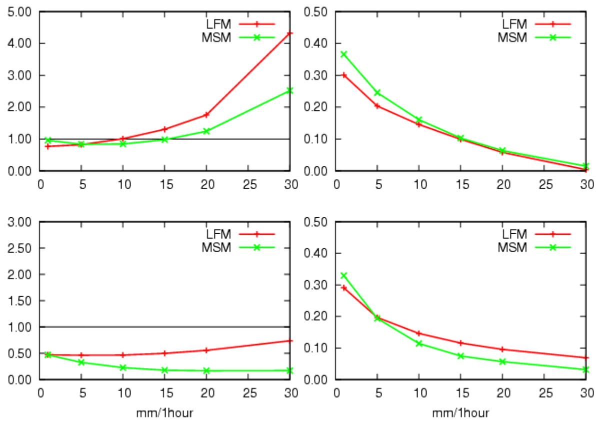

Fig 1. The bias score and the equitable threat score of precipitation forecasts against the Radar-raingauge Analyzed Precipitation for the period from June 2007 to December 2007. The red line indicates the LFM and the green line indicates the MSM. Left : bias score, Right : equitable threat score. Upper : average, Lower : maximum, both in every 20 km square mesh over land and over sea near the coast.

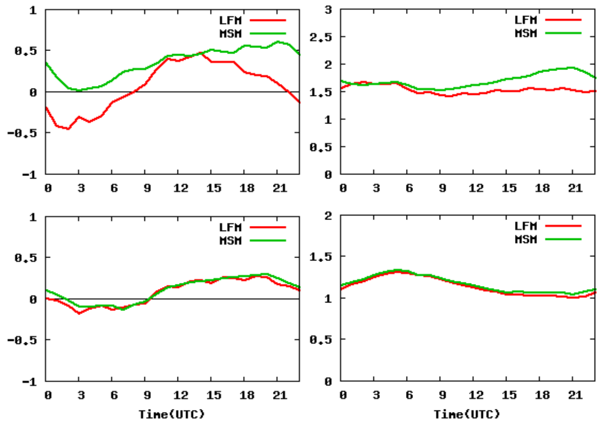

Fig 2. The Diurnal Change of the mean error (ME) and the root mean square error (RMSE) of surface temperature and surface wind speed forecasts against the AMeDAS data of about 80 points in the domain for the same period as Figure 1 (03 UTC is noon and 15 UTC is midnight at local time). The red line indicates the LFM and the green line indicates the MSM. Left: ME, Right: RMSE, Upper: surface temperature, Lower: surface wind speed.

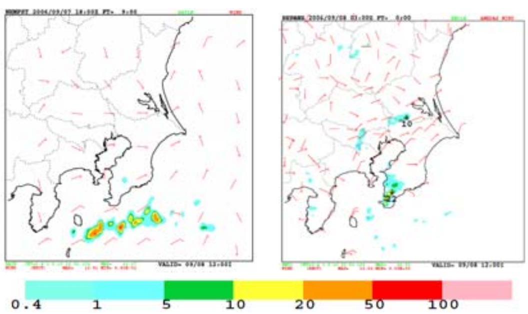

Fig 3. The 1-hour accumulated precipitation (mm/hr) and the surface wind (Each full wind barb is 10kt and each half-barb is 5kt.) at 03 UTC on 08 September 2006. Left : the LFM (Initial time = 18UTC, Forecast time = after 9 hours, without convective parameterization), Right : The Radar-raingauge Analyzed Precipitation and the surface wind observed by the AMeDAS.

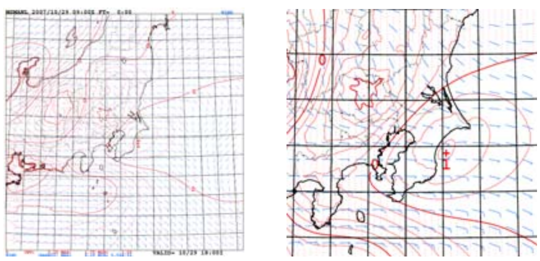

Fig 4. The analyzed increments of the surface temperature and the surface wind in a rapid update cycle at 09 UTC on 29 October 2007. The spacing of isoline is 0.2 degrees, the hatched area indicates the area which has negative increment on temperature. Each full wind barb is 2 m/s and each half-barb is 1 m/s. Right : the zoomed-in image of the central portion of the Left image.

On the phase and amplitude of shear-induced wavenumber-one convective asymmetry in the inner-core region of tropical cyclones

Mitsuru Ueno
Typhoon Research Department, Meteorological Research Institute
e-mail: mueno@mri-jma.go.jp

It is well known that mature tropical cyclones exhibit highly axially symmetric structure in the core with respect to the center. On the other hand, previous observational and numerical studies have shown that convective activities tend to be enhanced on a side of the eyewall rather than evenly significant in the eyewall annulus. Some of the studies attributed the convective asymmetry to the ambient vertical wind shear in which the storms were embedded. However, the precise mechanisms by which the environmental shear controls the convective asymmetry are not yet clearly established. In the present study, the factors to determine the phase and amplitude of wavenumber-one vertical motion asymmetry are investigated separately for each of the phase and amplitude.

As for the amplitude, a simple analytical formula for the magnitude of shear-induced wavenumber-one vertical motion at the radius of maximum wind was derived as a function of both the shear and storm strengths, based on the thermal wind balance consideration (Ueno 2007a). To examine the validity of the derived analytical formula, a set of idealized numerical experiments were performed (ditto). It was found from the validation study that very high correlation coefficients are calculated between rainfall asymmetry and analytical vertical motion, suggesting that both the shear and storm strengths are dominant factors in determining the magnitude of rainfall asymmetry. In the present study, the validation is extended to a real data simulation for the case of Typhoon Chaba in 2004. Figure 1 compares the analytical vertical motion with the simulated one over the entire integration period. Although the analytical formula tends to significantly underestimate the simulated omega due to diabatic enhancement of simulated vertical motion fields, the correlation coefficient between analytical and simulated omega is as high as 0.78, while that between shear itself and simulated omega is 0.44. Higher coefficient for the analytical omega is consistent with Ueno (2007a) and confirms that the vortex structure parameters as well as shear are contributing factors to the vertical motion asymmetry.

As for the phase, it is known from previous observational and numerical studies that convective activities tend to be enhanced on the downshear-left side of storms rather than just downshear. To discover the processes that govern the directional preference, a Lagrangian trajectory approach is applied to the numerical model data. The results suggest that asymmetric water vapor distribution caused by shear-forced vertical motion is a primary factor to locate the rainfall maxima on the downshear-left side rather than right downshear of the storm center. Figure 2 shows a horizontal plan view of net moisture changes due to vertical motion and diabatic processes (left) and resultant moisture asymmetry (right) at a midtropospheric level. While moisture increase tends to occur downshear due to shear-induced upward motion there, high moisture area is found about 90° of azimuth counterclockwise from the azimuth of the net moistening maximum (i.e., on the downshear-left side) due in part to horizontal advection. The moisture asymmetry could account for the simulated convective asymmetry. Details of the present study can be found in Ueno (2007b).

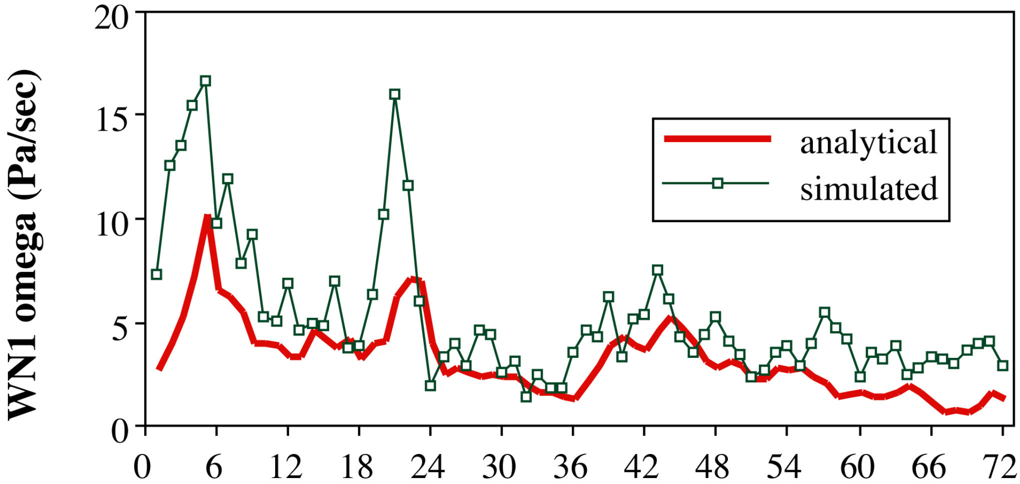

Figure 1: Comparison of "analytical" (thick red line) and model-simulated (thin green line with open squares) wavenumber-one omega (i.e., vertical p-velocity in units of Pa s^{-1}) at RMW and at 700 hPa. The horizontal axis denotes the integration time.

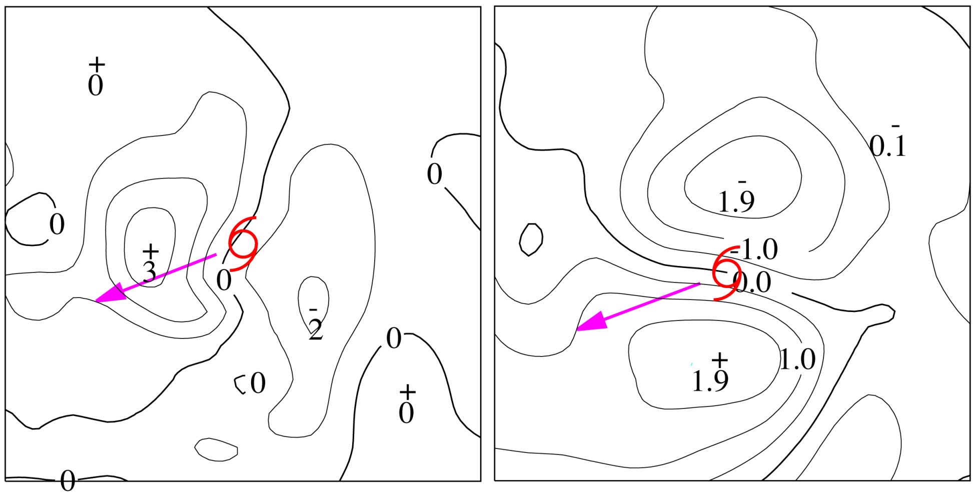

Figure 2: 6-hour composite from 24 to 30 h of simulation for specific humidity change at 5350 m due to vertical motion plus diabatic processes in units of g Kg^{-1} h^{-1} (left) and asymmetric specific humidity field at the same altitude in units of g Kg^{-1} (right). Plotted domain is 280 km x 280 km in size and the arrow indicates the direction of mean shear vector during the period.

References

Ueno, M., 2007a: Observational analysis and numerical evaluation of the effects of vertical wind shear on the rainfall asymmetry in the typhoon inner-core region. ***J. Meteor. Soc. Japan*, 85**, 115-136.

Ueno, M., 2007b: Effects of ambient vertical wind shear on the inner-core asymmetries and vertical tilt of a simulated tropical cyclone. Submitted to ***J. Meteor. Soc. Japan.***